CΦxford Physics

C4: PARTICLE PHYSICS MAJOR OPTION

PARTICLE DETECTORS

Author: William Frass   *Lecturer*: Dr. Roman Walczak   Michaelmas 2009

Contents

w.frass@seh.oxon.org

1 Introduction

1.1 The aims of particle detectors

The aim of a particle detector is to quantify the momenta and discover the identity of the particles that pass through it after being produced in a collision or a decay - an '**event**'.

The event might be a collision deliberately engineered to occur within the detector leading to many particles which in turn decay into many more, or it could be a decay that occurs naturally (in the upper atmosphere, for example), which is then detected on Earth. The exact position in space where the event occurs is known as the **interaction point**.

In order to identify every particle produced by the collision, and plot the paths they take - to '**completely reconstruct the event**' - it is necessary to know the mass and momentum of the particles. The mass can be found by measuring the momentum and either the velocity or the energy.

The modern large-scale detectors used today at places such CERN, including ATLAS and LCHb, which encompass many forms of tracking chambers and calorimeters that completely surround the interaction point are known as '**hermetic detectors**'.

1.2 Momentum determination

A **tracking detector** reveals the path, or '**track**', taken by a particle. Momentum measurements can be made by applying a magnetic field perpendicularly to the direction of travel in a tracking detector, this causes the particle to curve into a circular orbit with a radius proportional to the momentum of the particle; consider the Lorentz force on the particle:

$$F = qvB \tag{1}$$

$$ma = qvB \tag{2}$$

$$m\left(\frac{v^2}{r}\right) = qvB \tag{3}$$

$$\frac{mv}{r} = qB \tag{4}$$

$$r = \frac{mv}{qB} = \frac{p}{qB} \tag{5}$$

$$r \propto p \tag{6}$$
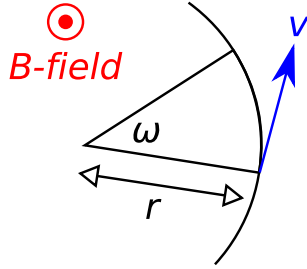
Figure 1: *A particle with velocity v entering a magnetic field. In unit time the particle travels a distance v around the circle and turns through an angle ω.*

The radius is also proportional to the mass-charge-ratio, m/q, so if two particles have the same speed, and one is half as heavy as the other, but has twice the charge, they will both orbit with the same radius.

Since the magnetic field exerts a force perpendicular to the direction of the particle's direction, it can do no work on the particle, hence the particle does not lose energy as a result of this process.

Thus having established the momentum, the energy can be measured by a calorimeter and the mass of the particle, and hence its identity, deduced.

The direction the particle curves in the magnetic field reveals its charge, since positive and negative charges curve in opposite directions.

1.3 Energy determination

Calorimeters rely on energy loss phenomena in order to determine the energy of the particles passing through them. In the case of detectors built specifically for calorimetry, the energy deposition is usually in the form of electromagnetic or hadronic showers, however calorimeters exist that exploit completely different forms of energy loss. In addition, a tracking detector is sometimes also able to provide information on energy loss.

1.4 Spatial resolution

The term **spatial resolution** has a dual meaning in the context of tracking detectors:

- The precision with which a tracking detector reports the true location of a particle. The usual measure of this precision is the square root of the variance of the probability density function that gives the probability of getting a signal for a particle at x when it has crossed the detector at x':

$$\sigma(x') = \left[\int (x - x')^2 P(x, x')dx \right]^{1/2} \approx \left[\int (x - x')^2 \times r'(x - x')dx \right]^{1/2} \tag{7}$$

- The ability of a tracking detector to distinguish the signals it receives due to two different particles passing very close to each other.

Spatial resolution is also significant, albeit slightly less important, in calorimeters. This is because in large hermetic detectors it is often necessary to associate a particle's calorimeter hits with the track it has left in tracking detectors - for this to work, the calorimeter has to be able to report fairly accurately where the energy was deposited.

1.5 Temporal resolution

The **time resolution** of a detector determines how well it is able to distinguish two events which happen in quick succession. It is important to have good time resolution for fast-triggering applications such as time of flight measurements. As in the case of the spatial resolution, the temporal resolution is measured using the standard-deviation (the square root of the variance).

The temporal resolution can be influenced by many properties of the detector, not limited to the material it is made from, the size and the surface of the scintillation counter and the properties of the light guide.

1.6 Typical spatial and temporal resolutions for common detectors

Typical values of spatial and temporal resolutions for various common detectors are given below: [1]

Detector type	Spatial resolution [μm]	Temporal resolution [ns]
Bubble chamber	$10 - 150$	1×10^6
Spark chamber	300	2000
Proportional chamber	$50 - 300$	2
Drift chamber	$50 - 300$	2
Liquid argon drift chamber	$175 - 450$	200
Scintillator (refractive index n)	—	$0.1/n$

The bubble chamber is now obsolete, but has been included in a few tables for comparative purposes.

---

[1] Source: Table 28.1 of Particle Data Group 2008.

2 Gaseous ionisation detectors

2.1 Principle of operation

The principle on which gaseous ionisation chambers work is outlined below:
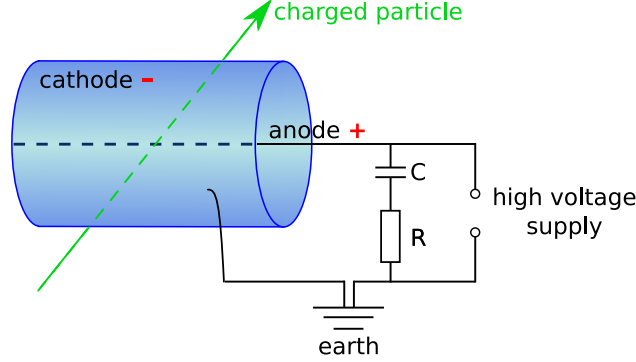

Figure 2: Circuit diagram for a gaseous ionisation chamber.

A voltage is applied to the central anode (positive) and the chamber walls / cathode (negative) to create an electric field between them. When a charged particle passes through the chamber it ionises the gas molecules inside, along the path it takes, creating negative electrons (anions) and positive ions (cations).

The collection of these charged particles reduces the voltage across the capacitor - this in turn increases the voltage across the resistor. This '**pulse**' across the resistor is recorded electronically, registering a hit.

The height of the pulse can be calculated as follows:

- The charge, Q on a capacitor of capacitance C under voltage V is given by:

$$Q = CV \tag{8}$$

- As mentioned above, a change in the charge causes a change in the voltage:

$$\Delta V = \frac{\Delta Q}{C} \tag{9}$$

- The change in charge is equal to the number of electrons collected by the anode. This is related to the number of ionising events that occur, n, as the charged particle being detected passes through the gas. If the ionisation products have sufficient energy to cause secondary ionisations, then the charge due to the primary ionisation events ($n \times e$) must be multiplied by the gas amplification factor A:

$$\text{Pulse height} = \Delta V = \frac{A\,n\,e}{C} \tag{10}$$

- The gas amplification factor, A, is dependent on the voltage applied.

Many different elements or compounds can be used to fill the chamber[2] - but they are **always gases** because the ionisation products can move to the relevant electrodes more easily in a gas than they can in a liquid or solid.

As shown in equation (10), the pulse height is dependent on the number of ion pairs collected by the anode. However, the number of ion pairs collected varies hugely depending on the applied voltage. So much so, that the way a detector behaves is different in each of the voltage ranges.

---

[2]Examples include helium, argon and boron triflouride.

2.2 Applied detector voltage

The number of ion pairs collected varies hugely as the voltage applied to the detector (see Figure 2) is increased. The graph below shows two curves, the curve for alpha-particles is higher than the curve for beta-particles because of the greater number of initial ion pairs an alpha-particle is able to produce due to its larger mass.
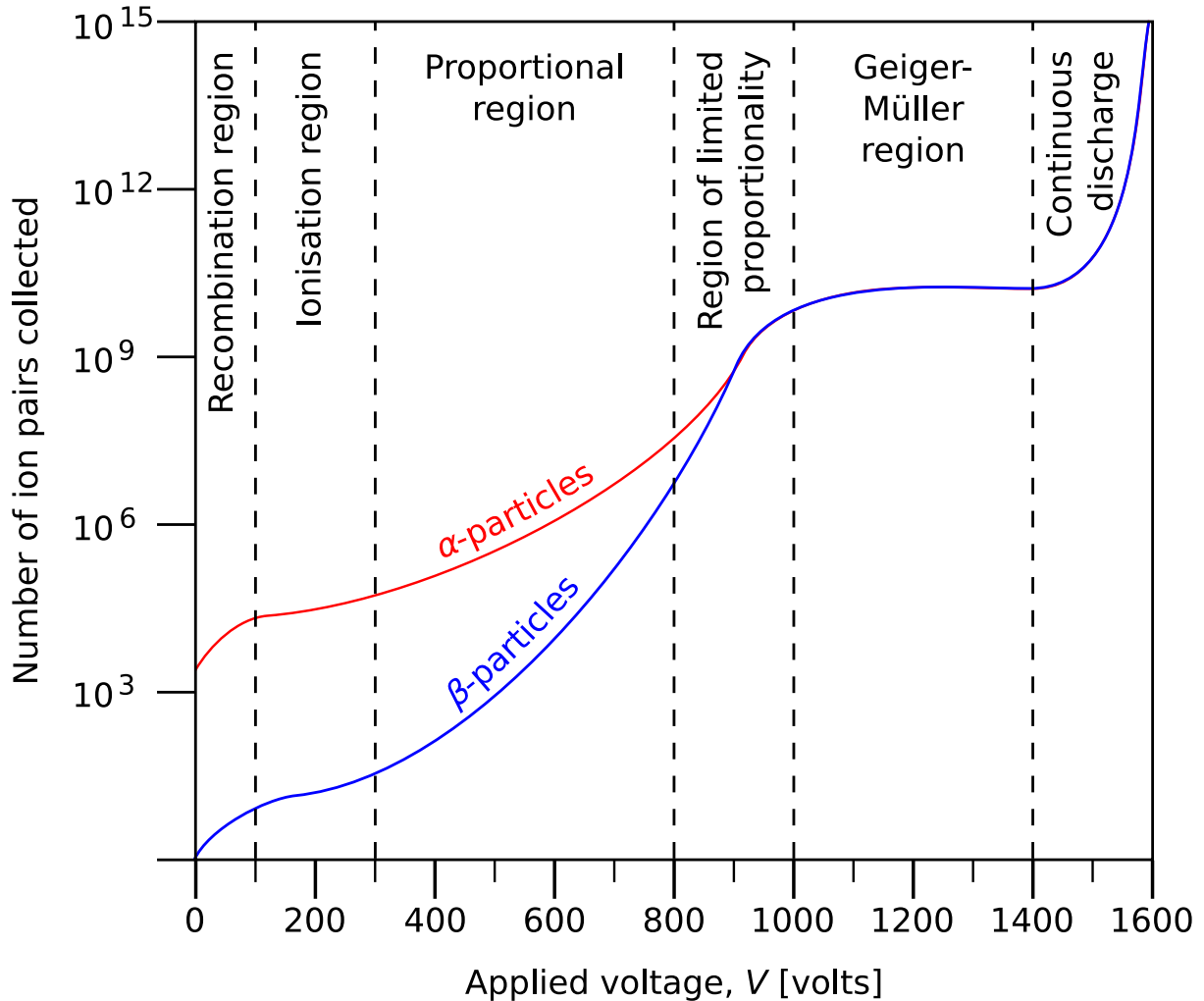
Figure 3: Number of ion pairs collected versus applied voltage in a gaseous ionisation chamber.

Recombination region

In this region, the voltage is insufficient to create an electric field strong enough for collection of all the ions produced. Instead they drift too slowly towards the electrodes and recombine back to neutral molecules before they can be collected. Obviously as the voltage is increased - more ions are collected, but until the saturation value is reached, not all ions will be prevented from recombining. For this reason gaseous ionisation chambers are not operated at these voltages.

Ionisation region

Somewhere around 100 V a **saturation** value is reached: the voltage is now sufficient to ensure collection of all the ion pairs that the charged particle creates. However, the voltage is not yet strong enough to cause secondary ionisation - there is no gas amplification here, hence there is no rise in the number of ions collected.

Proportional region

The voltage in this region produces a large potential gradient near the anode. Gas amplification is now possible because the electrons produced by ionisation are accelerated up to speeds where they can cause secondary ionisation - this is a **Townsend avalanche**. In this region the voltage pulse is **proportional** to the amount of ionisation.

Region of limited proportionality

As the voltage is increased further, the strength of the electric field causes electrons to be released from the cathode. This results in the Townsend avalanche spreading along the anode, whilst the positive ions then tend to remain near where they were created. This reduces the electric field to a point where further ionisation events are impossible: the number of ions pairs collected begins to level off again. This is another range of voltages not used for detectors.

Geiger-Müller region

By this point the voltage is so high that once an avalanche is initiated, it continues to spread until gas amplification becomes impossible due to a build-up of positive ions around the anode forming a dense shield. Once the **threshold** has been crossed and the dense shield is formed, no more ions can be collected and the graph reaches the **Geiger plateau**.

The number of ions required to shield the anode depends on the detector and not the charged particle passing through it. Therefore both alpha- and beta-particles have the same Geiger plateau because once the ion shield is in place, no more ionisation events can occur, irrespective of the charged particle under detection.

Region of continuous discharge

Finally, if the voltage is increased further it is so high that once ionisation occurs there is a continuous discharge of electricity. The Geiger plateau is the last useful range for continuously applied voltages - anything above this cannot be used for particle detection.

Spark chambers do operate at voltages above those shown on the graph - but there is a single discharge onto the plates - not a continuous voltage supply.

2.3   Detectors working in the ionisation region: ionisation chambers

Ionisation chambers operate at the lowest possible voltages, in the ionisation region. Voltages lower than these are not sufficient for collection of all the electrons and some recombine with ions to form neutral atoms. The gas filling the chamber is often simply **air**. There are two types of ionisation chambers:

- **Pulse counting ionisation chambers:** each individual particle traversing the detector creates a pulse, which is counted.

- **Integrating ionisation chambers:** all the pulses add and the integrated total of all the ionisation events over a period of time is measured. This type is more commonly used.

There are also two possible geometries for ionisation chambers:

- **Parallel plates:** this design is preferred because it has a well-defined active-volume.

- **Concentric cylinders:** this design necessitates some insulator to support the central anode. A build-up of ions on this insulator will distort the electric field; this variation in the field means there is not a well-defined active-volume.

Ionisation chambers primarily detect charged particles through their ionisation losses. However they can also detect neutral photons and neutrons:

- **Photons** can be detected because the interactions they undergo, namely photoelectric emission, Compton scattering and pair production, all lead to the production of electrons, which are then detected in exactly the same way as the electrons resulting from an ionisation event.

- **Neutron** detection is not possible in an ordinary ionisation chamber because neutrons are not ionising. However, with the addition of a thin boron coating on the inner chamber walls, or the use of boron triflouride gas, the following reaction takes place:

$$^{10}_{5}\text{B} + {}^{1}_{0}\text{n} \rightarrow {}^{7}_{3}\text{Li} + {}^{4}_{2}\text{He} + 5\,\text{e} \tag{11}$$
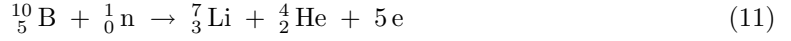
  The neutron is captured by the boron atom and an energetic alpha particle is emitted along with some electrons. The alpha particle is heavily ionising - losing all its energy in a just a few centimetres - allowing the neutron to be detected.

Such ionisation counters are widely used in the nuclear industry. By reducing the volume or decreasing the pressure inside the chamber, the active-volume is too small to contain the electrons produced by gamma radiation, so only the alpha-particles due to the presence of neutrons are counted.

Ionisation chambers are not really useful for modern particle physics experiments because they need heavy ionisation in order to receive a signal, yet fast particles create little ionisation according to (12), and they have a slower response time than proportional chambers. They do however, have a longer life-time than both proportional chambers and Geiger-Müller tubes because the gas in these tends to break down eventually.

2.4   Detectors working in the proportional region

2.4.1   Proportional chambers

Increasing the voltage from the ionisation region to the proportional region means gas amplification becomes possible. Amplification factors can be as high as 10^4, making **proportional detectors** much more sensitive than ionisation chambers because low energy ($E < 10$ keV) particles will still register due to the Townsend avalanches they create.

The voltage is large enough to collect all the electrons within microseconds. The height of the voltage pulse in a proportional chamber provides information about the energy of the incident charged particle:

$$\begin{pmatrix} \text{pulse} \\ \text{height} \end{pmatrix} \propto \begin{pmatrix} \text{charge} \\ \text{collected} \end{pmatrix} \propto \begin{pmatrix} \text{number of primary} \\ \text{ionisation electrons} \end{pmatrix} \propto \begin{pmatrix} \text{energy deposited by} \\ \text{the charged particle} \end{pmatrix} \propto \frac{1}{\beta^2} \tag{12}$$

This is the biggest advantage proportional chambers have over other gaseous ionisation detectors - in addition to tracking, they can provide information on the energy deposited by particles, which can be used for **particle identification**. This works because the geometry of the detector is such that the electric-field is insufficient to accelerate the electrons until they are micrometres from the anode: this way all electrons generate the same sized avalanche - no matter how far they have drifted before getting close to the anode.

The energy a particle deposits is, of course, proportional to $1/\beta^2$ according to the Bethe formula. Once the value of β is known, the energy can be found, if the momentum is deduced from magnetic curvature.

Unfortunately, for every electron there is an ion of chamber gas, which will gain an electron at the cathode and thus emit a photon. All these emitted photons release electrons from the cathode via the photoelectric effect, which will create unwanted pulses and could result in a current strong enough to melt the wire. These photons must be absorbed by a **quencher gas**, typically **carbon dioxide** or an organic molecule such as **methane**. A typical gas composition for proportional chambers is P-10 comprising 90% **argon** and 10% **methane**.

Spatial dependence of the voltage pulse

- The work done (ΔW = Force $\times$ distance), by a charge q moving through an electric-field, $\mathbf{E}$ is:

$$\Delta W = \int_{\text{start}}^{\text{end}} q\mathbf{E} \cdot d\mathbf{r} \tag{13}$$

- This change in energy is the source of the voltage pulse, ΔV. Voltage is the energy per unit charge, therefore the change in energy equals $Q \times \Delta V$:

$$Q\Delta V = \int_{\text{start}}^{\text{end}} q\mathbf{E} \cdot d\mathbf{r} \tag{14}$$

- The total charge a capacitor of capacitance C can store is $Q = CV_0$, with V_0 the applied voltage:

$$\Delta V = \int_{\text{start}}^{\text{end}} \frac{q}{CV_0}\mathbf{E} \cdot d\mathbf{r} \tag{15}$$

- $\mathbf{E}$ is sometimes expressed as the gradient of the potential, and in any case is given by **Gauss' law**:

$$\boxed{\text{Voltage pulse} = \Delta V = \int_{\text{end}}^{\text{start}} \frac{q}{CV_0}\frac{dV_0}{dr}\, dr} \tag{16}$$

- Recall the electric-field is not strong enough to cause an avalanche until the initial electrons are a small distance from the anode - call this distance λ. Integrating along their paths, it can be shown that the voltage pulse due to the electrons moving from λ to the anode is small compared to the pulse due to the ions moving from λ to the cathode: **the pulse is almost all due to the motion of the positive ions**.

Time dependence of the voltage pulse

- To find the temporal variation of the voltage pulse, substitute dV_0/dr for the electric field in (16).

- Now integrate (16), in general this time, using a boundary condition to find the constant of integration. This gives the voltage pulse in terms of r, hereby referred to as $\Delta V(r)$.

- The variable of time is introduced by considering the **drift velocity**. In a proportional chamber the drift velocity is proportional to the electric-field:

$$\boxed{\frac{dr}{dt} = v = \mu E} \tag{17}$$

- Substitute for the electric field, E, in (17) and integrate (17) with respect to time; this yields a new expression for r in terms of t. Now substitute this new expression into $\Delta V(r)$ giving $\Delta V(t)$.

- For the specific case of concentric cylinders of length l, with an inner cylinder having radius a:

$$\Delta V(t) = \frac{-Q}{4\pi\epsilon_0 l} \ln\left(1 + \frac{\mu CV_0}{\pi\epsilon_0 a^2}t\right) \qquad\qquad \Delta V(t) \propto \ln\left(1 + \frac{t}{t_0}\right) \tag{18}$$

- The constant t_0 is typically a few nanoseconds and depends on the geometry and ion mobility.

Dead time

- The longer the pulse, the longer the time before an individual wire can be used to detect another particle - the wire's **dead time**. The table below shows the dead time of some common detectors:[3]

	Bubble chamber	Spark chamber	Proportional chamber	Drift chamber	Scintillator
Dead time	50 ms	100 ms	200 ns	100 ns	10 ns

[3]Source: Table 28.1 of Particle Data Group 2008.

2.4.2 Multi-wire proportional chambers (MWPCs)

The detectors discussed so far have primarily been counters - they merely detect the presence of a particle. The proportional chamber advances this by virtue of the fact the voltage pulse it measures is able to provide information on the particle's energy as well.

The **multi-wire proportional chamber** or MWPC advances this further - instead of having one anode wire surrounded by a cathode wall or plate, multiple 'sense wires' are equidistantly spaced symmetrically between two parallel plates. Wire spacings are typically a few **millimetres**. A nearly uniform electric-field develops between the cathode plates, distorted only near the sense wires.

Each wire acts as a separate counter - when a charged particle passes through the chamber leaving a trail of electron-ion pairs, the electrons drift to the **nearest wire** and cause a voltage pulse. By placing another such configuration at 90° to the first, thus forming a grid, and marking off the wires that produce a pulse, the path of the charged particle is revealed.

As explained in Chapter 1, applying a magnetic field perpendicular to the direction the particle is travelling in, will cause it to spiral due to the Lorentz force. This will reveal how the particle is charged and what its momentum is.

A typical gas composition for multi-wire proportional chambers is the 'magic gas' mixture comprising 75% argon + 24.5% isobutane + 0.5% freon.

2.4.3 Drift chambers

The resolution of multi-wire proportional chambers can be dramatically enhanced by taking into consideration the **time the electrons take to drift** from the point where they were liberated to the sense wire, where they are detected. Thus one can infer the distance at which the charged particle passed the wire. This improves the spatial resolution and allows for wider wire spacings on the order of **centimetres**. Wider wire spacings distort the uniform field less, but increase the drift time, hence these '**drift chambers**' are not ideal for use in colliders with high collision rates, or in triggers.

In order to calculate the distance an electron has travelled it is necessary to understand its velocity in the electric-field. The uniformity of the field must be more carefully controlled than it is in a multi-wire proportional chamber: to this end, the anode sense wires are alternated with cathode **field wires** that 'correct' the field distortion caused by the sense wires, restoring uniformity throughout the chamber.

Drift velocities under electric-fields

The graph below shows the drift velocities of common drift chamber gases as a function of the applied electric-field:
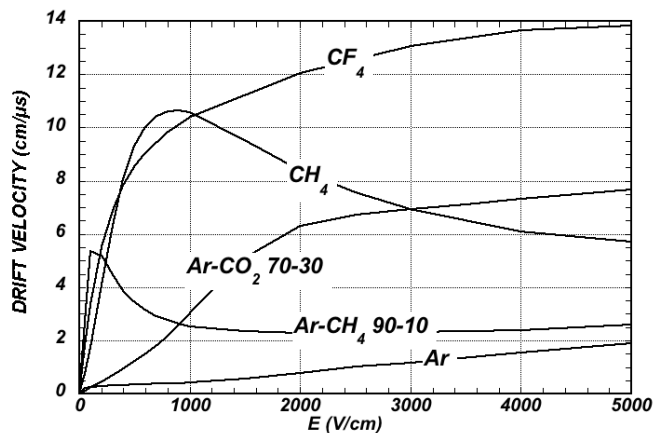

Figure 4: Computed electron drift velocity as a function of electric field in several gases at standard temperature and pressure. Taken from Figure 28.4 of the Particle Data Group 2008.

If the **average momentum relaxation time** is τ, then an electron moving in an electric-field E experiences a force:

$$F = \frac{dp}{dt} = \frac{mv_{\text{drift}}}{\tau} = eE \tag{19}$$

Here, v_{drift} is the **drift velocity of the electrons in an electric-field only**:

$$\boxed{v_{\text{drift}} = \frac{eE\tau}{m}} \tag{20}$$

Drift velocities under electric- and magnetic-fields

The situation becomes more complex upon the application of a uniform magnetic-field. The electrons now drift at an angle ψ with respect to the electric-field. If the electric- and magnetic-fields are perpendicular:

$$\boxed{\tan(\psi) = \omega\tau} \tag{21}$$

The angle ψ is known as the **Lorentz angle**, with the cyclotron frequency, ω, given by:

$$\omega = \frac{eB}{m} \tag{22}$$

In order to prove the relationship in (21), it is necessary to solve the equation of motion for an electron in both electric- and magnetic-fields. To avoid confusion with the electric-field-only drift velocity, v_{drift}, the symbol u will be used for the electric- plus magnetic-field case.

In addition to the Lorentz force, a particle in a gas filled drift chamber is also subjected to a retarding force proportional to its velocity $-K\mathbf{u}$:

$$m\frac{d\mathbf{u}}{dt} = e\mathbf{E} + e[\mathbf{u} \times \mathbf{B}] - K\mathbf{u} \tag{23}$$

The constant K is defined such that $\tau = m/K$. In steady-state (23) reduces to:

$$\frac{e}{m}\mathbf{E} = \frac{1}{\tau}\mathbf{u} + \frac{e}{m}[\mathbf{u} \times \mathbf{B}] \tag{24}$$

Writing out the x, y and z components of the above in a matrix equation gives:

$$\frac{e}{m}\begin{bmatrix} E_x \\ E_y \\ E_z \end{bmatrix} = \begin{bmatrix} 1/\tau & -\omega_z & \omega_y \\ \omega_z & 1/\tau & -\omega_x \\ -\omega_y & \omega_x & 1/\tau \end{bmatrix}\begin{bmatrix} u_x \\ u_y \\ u_z \end{bmatrix} \tag{25}$$

The ω components are defined according to (22). Solve for the drift velocity, $\mathbf{u}$, by inverting this matrix:

$$\begin{bmatrix} u_x \\ u_y \\ u_z \end{bmatrix} = \frac{\tau}{1 + (\omega\tau)^2}\begin{bmatrix} 1 + \omega_x^2\tau^2 & \omega_z\tau + \omega_x\omega_y\tau^2 & -\omega\tau + \omega_x\omega_z\tau^2 \\ -\omega_z\tau + \omega_x\omega_y\tau^2 & 1 + \omega_y^2\tau^2 & \omega_x\tau + \omega_y\omega_z\tau^2 \\ \omega_y\tau + \omega_x\omega_z\tau^2 & -\omega_x\tau + \omega_y\omega_z\tau^2 & 1 + \omega_z^2\tau^2 \end{bmatrix}\begin{bmatrix} E_x \\ E_y \\ E_z \end{bmatrix}\frac{e}{m} \tag{26}$$

This can be written in a more accessible form with the use of the unit vectors $\hat{\mathbf{E}}$ and $\hat{\mathbf{B}}$:

$$\mathbf{u} = \frac{eE\tau/m}{1 + (\omega\tau)^2}\left[\hat{\mathbf{E}} + \omega\tau(\hat{\mathbf{E}} \times \hat{\mathbf{B}}) + (\omega\tau)^2(\hat{\mathbf{E}} \cdot \hat{\mathbf{B}})\hat{\mathbf{B}}\right] \tag{27}$$

When $\hat{\mathbf{E}}$ is perpendicular to $\hat{\mathbf{B}}$ their scalar product is zero, so the last term vanishes:

$$\mathbf{u} = \frac{eE\tau/m}{1 + (\omega\tau)^2}\left[\hat{\mathbf{E}} + \omega\tau(\hat{\mathbf{E}} \times \hat{\mathbf{B}})\right] \tag{28}$$

Remember, ψ is the angle the electrons are drifting at with respect to the electric-field, in other words it is the angle between $\mathbf{u}$ and $\mathbf{E}$, readily found from $\mathbf{u} \cdot \mathbf{E}$:

$$\mathbf{u} \cdot \mathbf{E} = uE\cos(\psi) = \frac{eE\tau/m}{1 + (\omega\tau)^2}\left[\hat{\mathbf{E}} \cdot \mathbf{E} + \omega\tau(\hat{\mathbf{E}} \times \hat{\mathbf{B}}) \cdot \mathbf{E}\right] \tag{29}$$

The scalar product of a vector with its own unit vector returns the modulus of that vector ($\hat{\mathbf{E}} \cdot \mathbf{E} = E$). The second term is a triple-scalar-product, eligible for a cyclic-permutation:

$$uE\cos(\psi) = \frac{eE\tau/m}{1+(\omega\tau)^2}\left[E + \omega\tau(\hat{\mathbf{E}} \times \hat{\mathbf{E}}) \cdot \mathbf{B}\right] \tag{30}$$

The vector-product of a vector with itself is zero ($\hat{\mathbf{E}} \times \hat{\mathbf{E}} = 0$), hence the last term vanishes and some factors of E can be cancelled:

$$u = \sec(\psi)\frac{eE\tau/m}{1+(\omega\tau)^2} \tag{31}$$

Since electrons solely under the influence of an electric-field move in the direction of $\mathbf{E}$ and the Lorentz angle is the angle between $\mathbf{u}$ and $\mathbf{E}$ – ψ is also the angle between u and v_{drift}:

$$u = \cos(\psi)\, v_{\text{drift}} \tag{32}$$

Finally, substitute for u using (31) and for v_{drift} using (20):

$$\sec(\psi)\frac{eE\tau/m}{1+(\omega\tau)^2} = \cos(\psi)\,\frac{eE\tau}{m} \tag{33}$$

$$\sec(\psi)\frac{1}{1+(\omega\tau)^2} = \cos(\psi) \tag{34}$$

$$\sec^2(\psi) = 1 + (\omega\tau)^2 \tag{35}$$

$$1 + \tan^2(\psi) = 1 + (\omega\tau)^2 \tag{36}$$

$$\tan(\psi) = \omega\tau \tag{37}$$

This has important practical design consequences. For a typical gas the mean free path is 0.1 μm, and the argon-methane mix in Figure 4 has a drift velocity peaking at 5.5 cm/μs. This gives $\tau \approx 0.55$ ps. With a magnetic-field of 1 Tesla, $\tan(\psi) = 0.1$ or $\psi \approx 6°$. Drift chambers used with magnetic fields are often structured to follow the Lorentz angle.

2.4.4 Time projection chambers (TPCs)

A truly tridimentional reconstruction of an event can be made by recording both the radial (r) and azimuthal (θ) coordinates at which a charged particle enters and leaves a gas filled chamber using a multi-wire proportional grid arrangement at each end.

If a high-voltage cathode disc is placed at the centre of the chamber an electric-field can be established between the disc and the end-plates. The electrons that result from ionisation events in the chamber will drift to the multi-wire end-plates - a typical drift length is around 2 **metres**. The arrival times of the electrons at the end-plates determine how far they have travelled and hence the axial (z) coordinate of the charged particle, thus allowing it to be tracked along its journey through the chamber.

Additionally, a magnetic-field is often applied in the axial direction to minimise the diffusion of the electrons produced by the ionisation.

Finally, the velocity of the particle can be found if the two end-plates are used to trigger a timing device that records the time taken for the particle to travel the known length of the chamber. For this reason such detectors are called **time projection chambers** or TPCs.
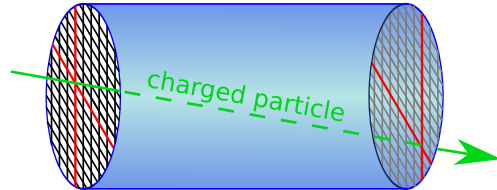

Figure 5: A time projection chamber. Those wires receiving hits are shown highlighted.

2.4.5 Brief history of improvements to the proportional chamber

Chamber type	Drift volume	Invented	Inventors
Multi-wire proportional chamber	$\sim$ mm	1968	Georges Charpak then at CERN was awarded the 1992 Nobel Prize in Physics "for his invention and development of particle detectors, in particular the multi-wire proportional chamber".
Drift chamber[a]	$\sim$ cm	1969	Bressani, Charpak, Rahm and Zupancic added a 3cm long drift space to a conventional 12×12 cm multi-wire proportional chamber at CERN.
Time projection chamber	$\sim$ m	1979	The time projection chamber was invented by David Nygren at the Lawrence Berkeley Laboratory. Its first major application was in the PEP-4 detector, which studied 29 GeV e^+e^- collisions at SLAC.

---

[a]Useful resource at Google Books: Particle Detection with Drift Chambers (W. Blum, W. Riegler & L. Rolandi)

2.5 Detectors working in the Geiger-Müller region

2.5.1 Geiger-Müller tubes

After the proportional region, a further increase in the applied voltage takes the graph into the region of limited proportionality, as the number of ion pairs begins to flatten out. The final useful region of applied voltage is the **Geiger plateau** - this is the region of operation of the **Geiger-Müller tube**.

Traditional Geiger-Müller tubes have a window at one end, trapping the **noble gas**[4], through which the charged particle may enter. Geiger-Müller tubes are only really used for nuclear work so are largely concerned with alpha, beta and gamma radiation. The window is made of either:

- **Glass-mantle:** thicker window, which is cheaper and stronger. However, alpha particles cannot penetrate the glass, so are not detected.

- **Mica:** thinner window, which is more expensive and fragile. But alpha radiation may be detected.

Neutron detection is possible using the boron trifluoride gas techniques discussed in conjunction with ionisation chambers.

For any given detector working in the Geiger-Müller region, all particles have the same Geiger plateau. Therefore the same number of ions are collected irrespective of the charged particle passing through the tube. This means the voltage pulse is the same height for all particles, making particle identification impossible. Despite this disadvantage Geiger-Müller tubes do produce many more electrons than detectors working in the proportional region and are thus more sensitive.

As with all detectors working above the ionisation region a **quencher gas** is necessary because of the positive ions produced by gas amplification.

2.5.2 Multi-wire chambers (MWCs)

Multi-wire chamber, or often just **wire chamber**, is the name used to refer to a multi-wire arrangement operated in the Geiger-Müller region, hence it can be considered an advancement on the Geiger-Müller tube. However, there is little point in building such a detector and then operating it in the Geiger-Müller region, when it could be operated at a lower voltage and have all the benefits of the multi-wire *proportional* chamber.

---

[4]Helium, neon and argon are all used.

2.6 Detectors working in the continuous discharge region: spark chambers

Spark chambers (or **streamer chambers**) are usually filled with **helium** or **neon**. They are gaseous ionisation chambers, but do not have a continuous supply of electricity. Instead a charged particle will trigger its own detection by passing through a scintillator at either end of the chamber. When the coincidence unit receives a signal from both of the scintillators' neighbouring photomultiplier tubes (PMTs) it triggers the discharge of many kilovolts onto the plates. Meanwhile the particle has left a trail of electrons and ions in the spark chamber itself. The now highly charged plates will seek to discharge themselves via the easiest route - in this case along the trail of electrons just left by the charged particle. Sparks fly between the plates with a loud crack showing the path the particle took.
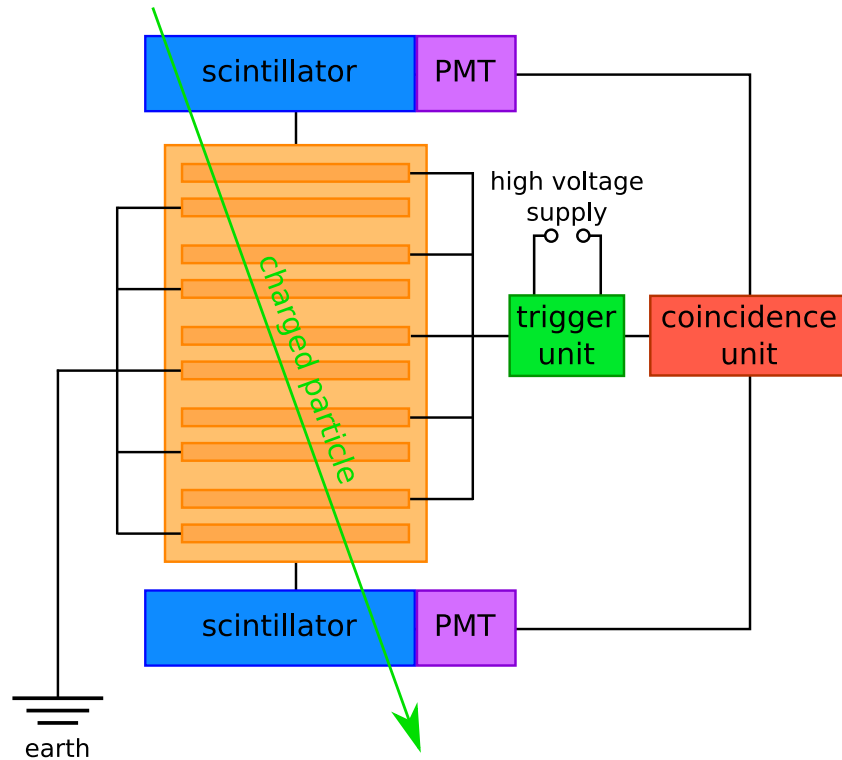

Figure 6: A spark chamber.

A more detailed explanation of spark formation is now given. The huge voltage difference across the plates accelerates the electrons so they are able to cause multiple secondary ionisations; an avalanche quickly forms. The electrons move to the head of the avalanche, positive ions move to the tail.

When sufficient electron-ion pairs have been created an electric-field forms within the avalanche itself, except this field points in the opposite direction to the one between the plates.

When the avalanche's field is strong enough, the electrons and ions recombine, leading to isotropic photon emission from the site of the avalanche. These photons cause ionisation in the vacinity of the avalanche - hence new avalanches rapidly form, merging with the original and eventually forming a conducting plasma between the two plates known as a **streamer**. Finally a spark travels between the two plates allowing the path the charged particle took to be visualised.
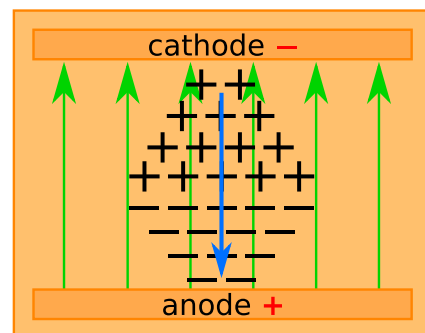

Figure 7: The electric field inside the avalanche points in the opposite direction to the chamber's electric field; eventually leading to recombination.

3 Solid state detectors

3.1 Silicon semiconductor detectors

3.1.1 Principle of operation

Most modern particle detectors use **silicon detectors** as their central tracking detector - the position resolution possible far exceeds that which is possible in gaseous ionisation chambers:

- An individual detector module comprises silicon that has been **doped** to form a diode.

- When the module is **reverse-biased**, a depletion region is set up with an electric-field that sweeps charge-carriers to the electrodes.

- When a charged particle passes across the silicon strip it will **liberate** electrons from their atoms creating **electron-hole pairs**. This is analogous to a charged particle creating electron-ion pairs when traversing a gas.

- The electric-field in the depletion region sweeps the new electron-hole pairs to the electrodes where they are **collected** and that particular module records a 'hit'.

- In contrast to gaseous detectors, silicon detectors do not track the charged particle through the entire body of silicon - instead **individual, isolated** mm sized **strips** or μm sized **pixels** record hits.

- Those modules that record hits trace out the path followed by the charged particle. The smaller the modules, the better the **spatial resolution**: around 5 μm for a 300 μm thick module.

The time taken for collection decreases as the bias voltage is increased. Increasing the voltage beyond that necessary for complete collection - **over-biasing** - reduces the collection time further. In a silicon detector 300 μm thick, electrons are collected in about 10 ns and holes in about 25 ns.
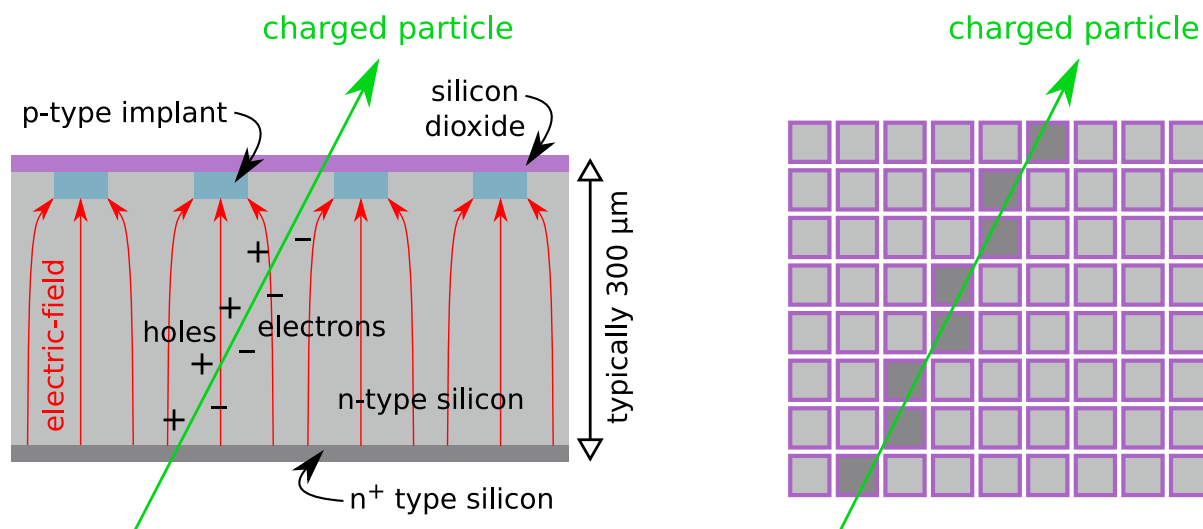
Figure 8: Left: schematic diagram of a silicon detector; Right: an array of silicon detector pixels - those which detected hits are shown highlighted and trace out the particle's trajectory..

In constrast to gasesous ionisation detectors, the active material in solid-state detectors is much **denser**, therefore every effort is made to make the silicon as **thin** as possible - otherwise any improvement in resolution gained by using silicon, is negated by the effects of increased **multiple scattering**.

Hence the increased spatial resolution possible with silicon detectors (compared to gaseous ionisation detectors) comes at an increased **cost**.

3.1.2 Energy resolution

If the band-gap energy required to promote an electron into the conduction band and create an electron-hole pair is E_{gap}, the number of electron-hole pairs produced by a particle despositing energy E is:

$$N = \frac{E}{E_{\text{gap}}} \tag{38}$$

Assuming a Poisson distribution for the number of electron-hole pairs, the fractional variance of N is:

$$\frac{\sigma_N}{N} = \frac{\sqrt{N}}{N} \tag{39}$$

The actual variance is affected by both electronic and lattice excitations. This is accounted for by the Fano factor, F ($F_{\text{Si}} \approx 0.1$):

$$\frac{\sigma_N}{N} = \frac{\sqrt{FN}}{N} = \sqrt{\frac{F}{N}} \tag{40}$$

This can be used to find the energy resolution by substituting from (38):

$$\boxed{\frac{\sigma_E}{E} = \sqrt{\frac{FE_{\text{gap}}}{E}}} \tag{41}$$

In actual fact, since silicon is an indirect semiconductor[5], E_{gap} should also include phonon excitation to provide the necessary momentum change. Taking this into account, at room temperature $E_{\text{gap}} = 3.67$ eV. Therefore a 1 MeV charged particle will produce about 272,000 electrons. This gives $\sigma_E/E = 0.06\%$.

However, the energy resolution is dominated by **electrical noise** and energy loss fluctuations in the detector, hence the need for expensive cooling and low-noise electronics.

3.1.3 Radiation degradation

There are two ways that radiation can degrade individual modules or clusters of modules:

Damage	Cause of damage and effect on module	Critical factors
Displacement	Displacement damage results from atoms being displaced from their lattice sites, leading to current leakage, free-carriers becoming trapped and a build-up of space charge (changing the required operating voltage).	Particle type + energy
Surface	Surface damage results from charge building up in surface layers, leading to surface current leakage meaning separate strips or pixels are no-longer isolated.	Radiation dose

3.2 Scintillators

3.2.1 Principle of operation

A charged particle passing through matter will create electron-ion pairs in a gas and electron-hole pairs in a semiconductor. In more complex substances however, the energy is manifest in excited molecules. Those substances in which the molecules de-excite by emitting a photon are known as **scintillators**.

If a photon excites the molecules of a substance, which then de-excite by emitting a lower energy photon, the substance is said to **fluoresce**. Absorption and emission occur over a wide range of photon energies, which can overlap, leading to unwanted self-absorption. The greater the difference between the main absorption and main emission energies (the Stokes' shift), the less the amount of self-absorption.

---

[5]The maxima of the valence band does not have the same k-space momentum as the minima of the conduction band

The organic substances used in detectors comprise a **mixture of both** scintillators and fluors. This is because typical scintillators emit ultraviolet light which is rapidly attenuated by the scintillator itself before it can ever be detected. The fluor acts as a **wavelength-shifter**: absorbing the ultraviolet light and re-radiating it as blue light (a wavelength at which the scintillator is more transparent). Sometimes secondary or even tertiary fluors are added to step-down the wavelength in stages.

If the fluor is added in high concentration the distance between the scintillator and the fluor is shorter than the wavelength of light. In these cases the energy transfer from scintillator to fluor occurs by dipole-dipole interactions, which are faster than absorption and emission, thus reducing the decay time by an order of magnitude.

3.2.2   Organic versus inorganic scintillators

The two main classes of scintillator are compared below:

Scintillator	Composition	Density	Examples	Notes
Organic	Carbon-based (often with benzene)	$1.03 - 1.20$ g cm^{-3}	Polystyrene polyvinyltoluene	Nearly all organic scintillators are plastic since it is cheap and easily moulded.
Inorganic	Non-carbon-based crystals	$4 - 8$ g cm^{-3}	Sodium iodide Barium fluoride	Higher density makes these useful for total absorption EM calorimeters (see § 4.2).

3.2.3   Organic scintillator photon yields and luminescence

On average one photon is emitted for every 100 eV of energy deposited in the scintillator. Therefore, a particle depositing 1 MeV will produce 10,000 photons. This gives $\sigma_E/E = 1\%$.

The luminescence of a scintillator, $\mathcal{L}$, is given by **Birk's Law**:

$$\frac{d\mathcal{L}}{dx} = \mathcal{L}_0 \left(\frac{dE/dx}{1 + k_B(dE/dx)} \right) \tag{42}$$

Here, $\mathcal{L}_l$ is the luminescence at low specific ionization density and k_B is the Birks constant for that particular scintillator.

3.3   Čerenkov detectors

3.3.1   Particle identification

By using a carefully chosen medium with the correct refractive index, particles can be distinguished by whether or not they emit Čerenkov radiation. The refractive index of a gas can be adjusted accordingly by varying the pressure.

There is a threshold velocity, and hence a threshold momentum below which particles do not radiate. This threshold is different for different particles. This is the principle of the **threshold Čerenkov detector**:

$$p = \gamma m v = \frac{m\beta c}{\sqrt{1 - \beta^2}} \tag{43}$$

Using the condition for Čerenkov radiation, $\beta = 1/n$, gives:

$$\boxed{p_{\text{threshold}} = \frac{mc/n}{\sqrt{1 - n^{-2}}}} \tag{44}$$

In an air filled detector ($n_{\text{air}} = 1.0003$) the threshold for pions is 5 GeV/c, but the threshold for kaons is 20 GeV/c. Therefore in the range 5 – 20 GeV/c pions radiate but kaons do not, allowing them to be distinguished. Below 5 GeV/c neither pions nor kaons radiate, and above 20 GeV/c they both radiate. The detector is therefore only useful in the range 5 – 20 GeV/c.

Modern Čerenkov detectors have 4π coverage of the radiating material with photomultiplier tubes. These detectors produce rings where the light-cone intersects the PMT-lined wall of the chamber and are known as **Ring Imagining Čerenkov detectors (RICH)**, see Section 7.3.

3.3.2 Calorimetry

Čerenkov detectors can be used as calorimeters because the amount of light produced is proportional to the total energy of the incident particle, E_0:

$$\text{(Amount of light)} \propto \int_0^{\text{track length}} \left(\begin{array}{c} \text{Number of emitting} \\ \text{particles at distance } L \end{array} \right) dL \tag{45}$$

The number of particles after N radiation lengths is 2^N. Convert the integral over dL to an integral over dN using the fact that the track length is the number of radiation lengths ($L = X_0 N \rightarrow dL = X_0 dN$). The integral's upper limit is now the number of radiation lengths at which the shower stops, N_C:

$$\text{(Amount of light)} \propto \int_0^{N_C} 2^N X_0 dN \tag{46}$$

$$\text{(Amount of light)} \propto X_0 \left[\frac{2^N}{\ln 2} \right]_0^{N_C} \tag{47}$$

$$\text{(Amount of light)} \propto \frac{X_0}{\ln 2} \left[2^{N_C} - 1 \right] \tag{48}$$

The critical value of N, namely N_C, can be converted into a critical energy. The initial energy E_0 is shared between however many particles there are after N radiation lengths:

$$E_N = \frac{E_0}{2^N} \qquad \rightarrow \qquad E_C = \frac{E_0}{2^{N_C}} \tag{49}$$

This means equation (48) can be re-written as:

$$\text{(Amount of light)} \propto \frac{X_0}{\ln 2} \left[\frac{E_0}{E_C} - 1 \right] \tag{50}$$

Finally, since $E_0 \gg E_C$:

$$\text{(Amount of light)} \propto E_0 \tag{51}$$

$$\boxed{\text{(Amount of light)} \propto \left(\begin{array}{c} \text{Energy of} \\ \text{incident particle} \end{array} \right)} \tag{52}$$

4 Calorimeters

4.1 Electromagnetic versus hadronic calorimeters

Calorimeters use partial or total absorption of particles and their showers to measure their energy. Calorimeters are typically composed of small **cells** aligned along the direction of the incident particle, stacked up in **towers**. The alignment of these towers usually varies around the detector in order to maximise the probability of encompassing the shower at a given angle.

Electrons, photons, and indeed π^0 mesons, which decay into photons, all produce electromagnetic showers. These showers are relatively compact and have a short shower-depth, therefore they are readily contained in a short distance by **electromagnetic calorimeters**. The size of an electromagnetic shower, and hence an electromagnetic calorimeter, is governed by the **radiation length**, X_0.

Hadronic showers are generally much larger and their shape fluctuates hugely from one event to another, hence **hadronic calorimeters** are larger than their electromagnetic counterparts. Indeed, the response is lower and the resolution is worse for hadrons in a hadronic calorimeter compared to electrons of the same energy in an electromagnetic calorimeter.

Most hermetic detectors use a calorimetry system that comprises both types of calorimeter. In such a **composite calorimeter** the electromagnetic calorimeter is always the first layer the particles encounter because whilst the heavy hadrons can pass through to the hadronic calorimeter beyond, electrons and photons would never reach their designated calorimeter if the hadronic calorimeter came first.

Although hadrons might start showering in the electromagnetic calorimeter, they can only be fully contained by the hadronic calorimeter. This is where all but the tiny fraction of energy hadrons lost in the electromagnetic calorimeter, is deposited.

In light of the above, the absorber material in an electromagnetic calorimeter should ideally maximise the hadronic interaction length (so as many hadrons can pass through with minimal interaction as possible) and minimise the radiation length (so the electromagnetic shower is fully developed within the electromagnetic calorimeter). The ratio λ/X_0 approximately satisfies: $\lambda/X_0 \propto Z^{1.3}$. Maximising this ratio means using **high-Z materials** like tungsten ($Z = 74$), lead ($Z = 82$) or uranium ($Z = 92$).

4.2 Homogeneous versus heterogeneous calorimeters

There are two parts to any calorimeter:

- **Active signal generators:** the active material that measures the shower energy.

- **Passive particle absorbers:** the material that causes the particles to shower.

Calorimeters can incorporate these two aspects in two different ways, contrasted below:

	Hetrogeneous or sampling calorimeters	Homogeneous calorimeters
Design	The active layers are **interleaved** with passive absorbers. However, it is only the small fraction of energy deposited in the active layers that is measured.	The roles of the active material and the passive absorber are **combined**.
Particles	The length and width of hadronic showers means hadronic calorimeters have to be of the sampling type, but electromagnetic calorimeters can also be sampling.	The materials suitable for both these roles can only be used in electromagnetic calorimeters.
Active	Solid or liquid scintillating material or some form of gaseous proportional counter.	Crystals like NaI, $Bi_4Ge_3O_{12}$ ('BGO') and CsI or composite materials such as lead-glass.
Passive	Sheets of high-Z materials such as lead or uranium.	

4.3 Energy resolution

The accuracy with which a calorimeter reports the energy of a particle is usually expressed as a fraction of the **particle's energy**, E, and comprises four separate contributions added in quadrature:

$$\left(\frac{\sigma}{E}\right)_{\text{total}} = \left(\frac{\sigma}{E}\right)_{\text{statistical}} \oplus \left(\frac{\sigma}{E}\right)_{\text{instrumental}} \oplus \left(\frac{\sigma}{E}\right)_{\text{systematic}} \oplus \left(\frac{\sigma}{E}\right)_{\text{sampling}} \tag{53}$$

The term **energy resolution** applies to the constant σ.

Contribution	Scales as	Origin of errors and their scaling	Energy range
Statistical	$\propto \frac{1}{\sqrt{E}}$	Showers are inherently statistical processes, thus the energy deposited varies according to a Poisson distribution: $\sigma/E = \sqrt{N}/N = 1/\sqrt{N}$. Since the energy deposited is proportional to the number of hits ($N \propto E$), this can be written as $\sigma/E \propto 1/\sqrt{E}$.	This contribution is the most significant and dominates over most of the useful range of calorimeters.
Instrumental	$\propto \frac{1}{E}$	The effect of noise and stray capacitance is largely energy independent, hence the relative contribution (σ/E) scales as $1/E$.	This contribution tends to dominate at low energies.
Systematic	constant	Systematic errors include calibration errors and non-uniformity of the calorimeter. Non-uniformity at high energies can limit accuracy to no-better than 2%. Usually, some average fraction of the energy leaks out of the calorimeter as it fails to completely contain the shower. These scale with energy, hence the relative contribution is energy independent.	This contribution usually sets the limit for performance at high energies.
Sampling	$\propto \sqrt{\frac{\Delta E}{E}}$	In sampling calorimeters the sampling fluctuations have to be added, with ΔE the energy loss of one particle in one layer.	This is only of significance in sampling calorimeters.

4.3.1 Electromagnetic calorimeters

In electromagnetic calorimeters the statistical errors result from variations in the track length of the charged particles:

$$\boxed{\left(\frac{\sigma}{E}\right)_{\text{statistical}}^{\text{electromagnetic}} \approx \frac{0.5\%}{\sqrt{E}}} \tag{54}$$

Some electromagnetic calorimeters are sampling calorimeters, for these the sampling fluctuations are given by:

$$\boxed{\left(\frac{\sigma}{E}\right)_{\text{sampling}}^{\text{electromagnetic}} \approx 4\% \sqrt{\frac{1000\Delta E}{E}}} \tag{55}$$

Total energy resolution below $\sigma/\sqrt{E} = 1\%$ is easily achieved in homogeneous electromagnetic calorimeters. Such results are more difficult to achieve in an electromagnetic sampling calorimeter.

4.3.2 Hadronic calorimeters

In hadronic calorimeters the statistical errors result from fluctuations in energy deposition due to energy loss through non-hadronic mechanisms such as photons and leptons from pion decay and slow neutrons. These fluctuations that arise in hadronic calorimeters are much larger than the main statistical errors in electromagnetic calorimeters:

$$\left(\frac{\sigma}{E}\right)^{\text{hadronic}}_{\text{statistical}} \approx \frac{45\%}{\sqrt{E}} \tag{56}$$

Compensating calorimeters are hadronic calorimeters with enhancements such as adjusted absorber layer and active layer widths and U-238 absorbers for slow neutron capture. These calorimeters reduce the statistical errors by around 20%:

$$\left(\frac{\sigma}{E}\right)^{\text{compensating}}_{\text{statistical}} \approx \frac{25\%}{\sqrt{E}} \tag{57}$$

All hadronic calorimeters are sampling, but the contribution to the total energy resolution due to sampling effects is small compared to the statistical errors:

$$\left(\frac{\sigma}{E}\right)^{\text{hadronic}}_{\text{sampling}} \approx 9\%\sqrt{\frac{1000\Delta E}{E}} \tag{58}$$

4.4 Typical energy resolutions for some calorimeters

Typical values of energy resolutions for various electromagnetic calorimeters are given below: [6]

Electromagnetic detector	Experiment	Energy resolution
Lead glass	OPAL	$5\%/\sqrt{E}$
Liquid krypton	NA48	$3.2\%/\sqrt{E} \oplus 0.42\% \oplus 0.09/E$
Liquid argon and lead	NA31	$7.5\%/\sqrt{E} \oplus 0.50\% \oplus 0.10/E$
Liquid argon and lead	ATLAS	$10\%/\sqrt{E} \oplus 0.40\% \oplus 0.30/E$
Depleted uranium scintillator	ZEUS	$18\%/\sqrt{E}$

Typical values of energy resolutions for various hadronic calorimeters are given below: [7]

Absorber and thickness	Plastic scintillator	Experiment	Energy resolution
6 mm uranium and 5 mm copper	2.5 mm	AFS	$35\%/\sqrt{E}$
80 mm marble	30 mm	CHARM	$45\%/\sqrt{E}$
25 mm iron	5 mm	CDHS	$58\%/\sqrt{E}$
50 mm iron	10 mm	UA-1	$80\%/\sqrt{E}$
15 mm iron	5 mm	UA-2	$60\%/\sqrt{E}$

---

[6]Source: Table 28.9 of Particle Data Group 2008.
[7]Source: Table 11.3 of Introduction to Experimental Particle Physics (R. Fernow).

5 Hermetic detectors

5.1 Introduction

The modern particle detectors in use today in accelerators such as the Large Electron Positron collider at CERN[8] or HERA[9] at DESY[10] are **hermetic detectors**. These are detectors designed to cover as much of the solid angle around the interaction point (**IP**) as possible – to **hermetically** encompass it. This is nearly always accomplished with a cylindrical **barrel** around the beam-pipe along which the accelerated particles travel with **end-caps** sealing in both ends of the barrel. The accelerators and detectors are often situated **underground** in order to provide the maximal shielding possible from natural radiation such as cosmic rays that would otherwise mask the events taking place inside the detector.

5.2 Layout and purpose of layers

Hermetic detectors combine many of the detectors discussed so far, such as the drift chambers, Čerenkov detectors, electromagnetic calorimeters and hadronic calorimeters. These are built up in **concentric layers**, with each layer designed to measure a specific aspect of the jets of particles produced after the collision at the interaction point. Starting with the innermost layer the successive layers in a hermetic detector are:

- **Central tracking detector (CTD):** this is designed to track all the charged particles and allow for complete event reconstruction.

- **Large magnet:** this produces a magnetic field strong enough to curve the tracks of charged particles in the tracking detector, allowing their momentum to calculated.

- **Electromagnetic calorimeter (ECAL):** this measures the shower energy of electrons and photons.

- **Hadronic calorimeter (HCAL):** this measures the hadronic shower energy.

- **Muon tracking chamber:** any particle registering on these tracking detectors (often drift chambers) has necessarily travelled through all the other layers and can only be a muon.
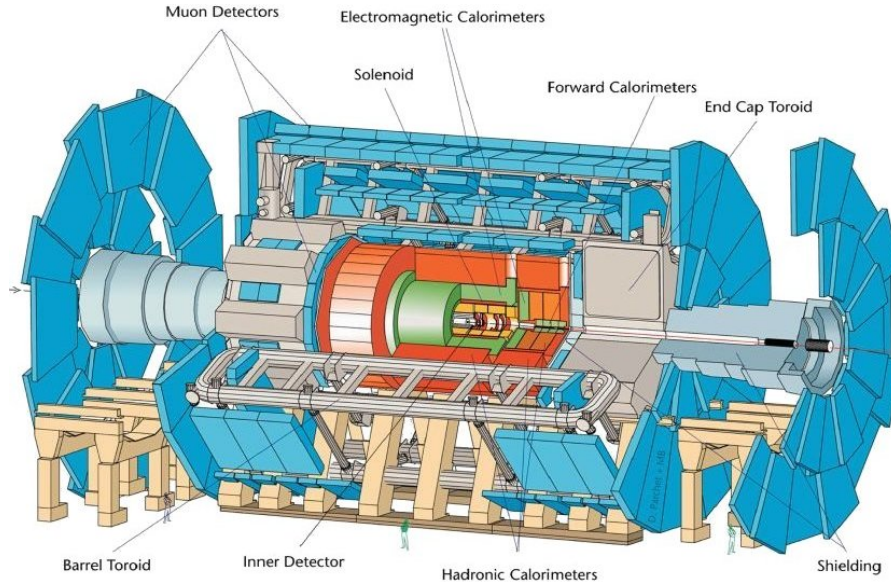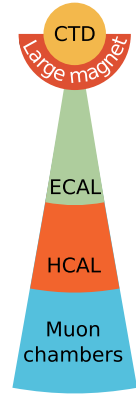

Figure 9: ATLAS (**A T**oroidal **L**HC **A**pparatu**S**) detector at CERN, a transverse slice is shown above.

---

[8]French: **C**onseil **E**uropeen pour la **R**echerche **N**ucleaire (European Council for Nuclear Research)

[9]German: **H**adron-**E**lektron-**R**ing**A**nlage (Hadron-Electron Ring Accelerator)

[10]German: **D**eutsches **E**lektronen **S**ynchrotron (German Electron Synchrotron)

5.3 Propagation of particles through the layers

Particles can be identified by their energy loss, curvature in magnetic fields and Čerenkov radiation. However, the identity of a particle can be significantly narrowed down by simply examining which parts of the detector it deposits energy in:

- **Photons (γ):** Neutral photons leave no tracks in the CTD but produce an electromagnetic shower in the ECAL.

- **Electrons and positrons (e^-, e^+):** Charged electrons and positrons leave tracks in the CTD and produce a shower in the ECAL.

- **Muons (μ^-, μ^+):** Muons leave tracks in all the detectors - they are the only particles to reach the muon chambers.

- **Charged hadrons (p, $\pi^\pm$, $K^\pm$):** Charged hadrons leave tracks in all the detectors up to the HCAL where they shower and deposit all their energy.

- **Neutral hadrons (n, K_L^0):** Neutral hadrons leave no tracks in any of the detectors and then they shower in the HCAL. K_S^0 mesons are not listed here because they decay before ever reaching the hadronic calorimeter.

A full description of the signature characteristic of all types of particle can be found in Section 7.1. For now, the above facts are summarised in the diagram below:
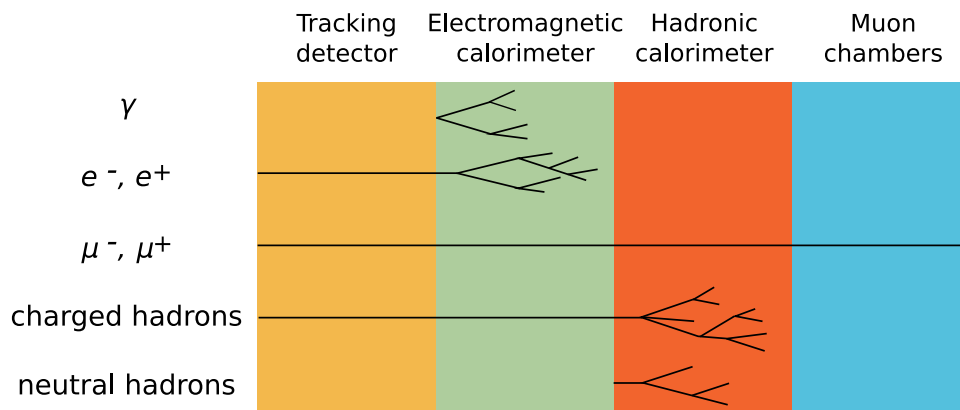

Figure 10: Overview of the signatures left in a hermetic detector by detectable particles.

6 Case studies
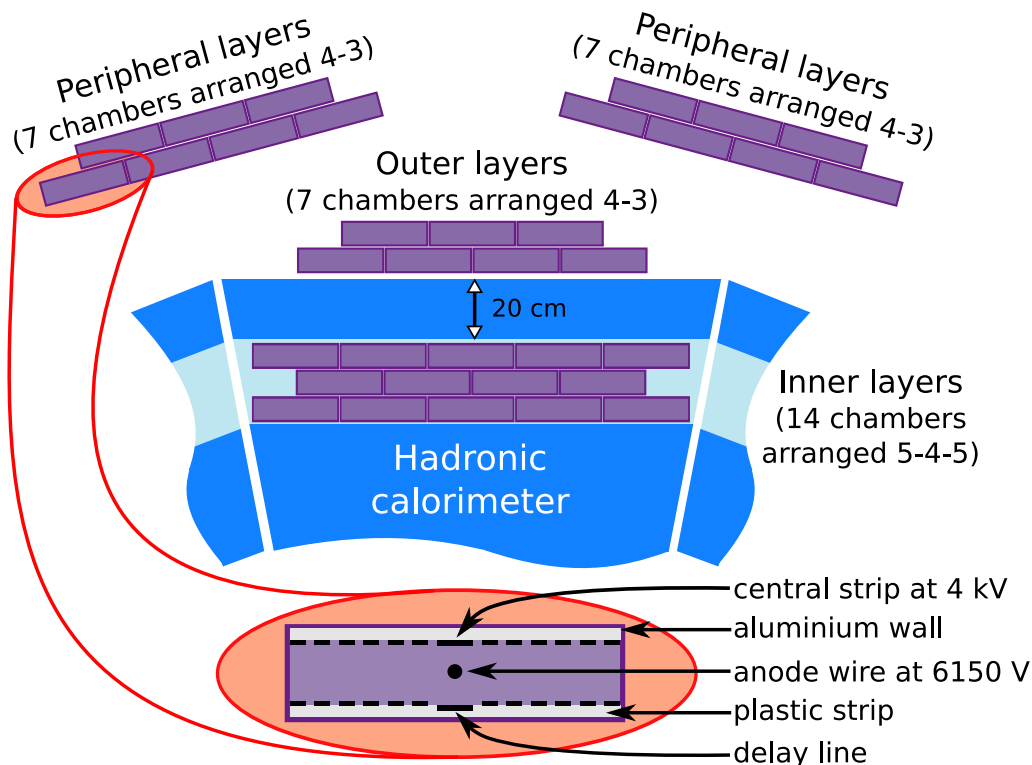
6.1 Drift chamber – barrel muon chambers at DELPHI

Figure 11: Diagram of a single sector showing the relative positions of the three layers in the barrel.

Overview of the barrel muon sector:

Dates:	Construction: $1983 - 1988$
	Operation: $1989 - 2000$
Drift chambers:	1372 chambers arranged into 24 sectors. Each sector contains an inner, outer and peripheral layer.

Details of the individual drift chambers:

Active volume:	$363 \times 20 \times 1.6 \, \text{cm}^3$
Gas mixture:	argon (84.6%)
	methane (8.9%)
	carbon dioxide (6.5%)
Field-strength:	$400 \, \text{V cm}^{-1}$
Drift velocity:	$46 \, \mu\text{m ns}^{-1}$
Spatial resolution:	$\sigma_{r\phi} = 1$ mm (drift time)
	$\sigma_z = 10$ mm (delay line)

Figure 12: The DELPHI detector. Some of the muon chamber detectors are visible. These are the long, flat, pieces of aluminium outside the hadron calorimeter.

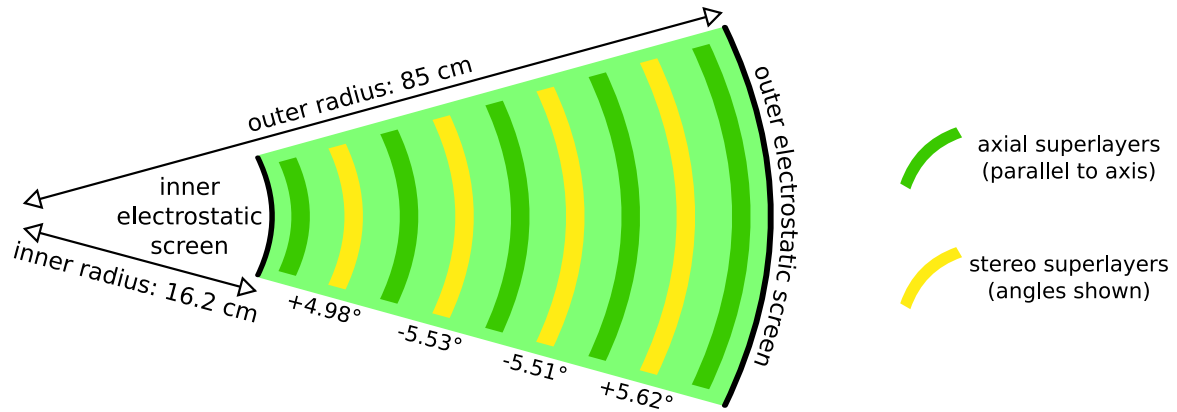## 6.2 Drift chamber with magnetic field – central tracking chamber at ZEUS

Figure 13: Diagram of the two types of superlayer within ZEUS' central tracking chamber.

Overview of the central tracking detector:

|	
Dates:	Operation: 1992 – 2007
Drift chambers:	576 drift cells arranged into 9 'superlayers'. Each drift cell has 8 sense wires and 34 field wires, giving a total of 4608 sense wires and 19,584 field wires.
5 axial superlayers:	Wires in these superlayers are parallel to the chamber axis.
4 stereo superlayers:	Wires in these superlayers are tilted by a small angle (5° or 6°) with respect to the beam and can thus provide information on the z-coordinate of the hits.
Active volume:	Length: 241 cm, inner radius: 16.2 cm, outer radius: 85 cm
Hermiticity:	Angles covered: $15° < \theta < 164°$
Gas mixture:	argon (90%) carbon dioxide (8%) ethane (2%)
Drift velocity:	50 μm ns^{-1}
Magnetic-field:	1.8 Tesla $\Rightarrow$ Lorentz $\psi \approx 45°$
Spatial resolution:	$\sigma_{r\phi}(\theta) = 0.1 - 0.2$ mm $\sigma_z = 2$ mm
Momomentum resolution:	$\frac{\sigma_p}{p} = 0.005p \oplus 0.007 \oplus \frac{0.001}{p}$ for p measured in GeV.
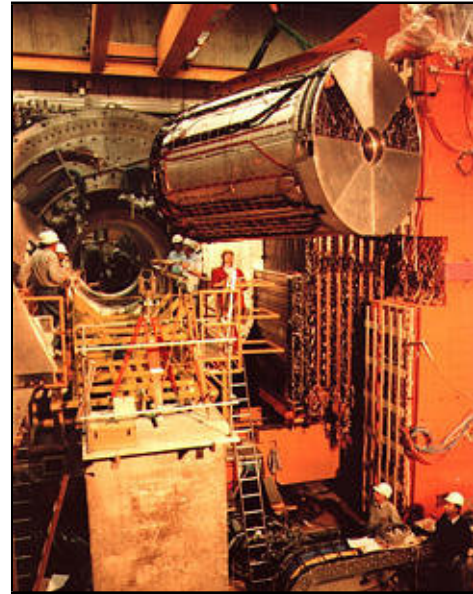
Figure 14: Installation of the central tracking detector at the heart of the ZEUS detector.

Figure 15: A view inside the chamber after the first of the superlayers had been 'strung'.

6.3 Sampling calorimeter − uranium-scintillator calorimeter at ZEUS

Overview of the uranium-scintillator calorimeter:

|	
Dates:	Operation: 1992 − 2007
Active material:	2.6 mm of plastic scintillator (SCSN38).
Passive material:	3.0 mm of uranium absorber (98.1% ^{238}U).
Chambers:	The UCAL comprises three main sections, divided into a total of 80 modules, further divided into towers - see the table below.
Hermiticity:	99.7%
Electromagnetic energy resolution:	$\frac{\sigma_E}{E} = \frac{18\%}{\sqrt{E}} \oplus 1\%$
Hadronic energy resolution:	$\frac{\sigma_E}{E} = \frac{35\%}{\sqrt{E}} \oplus 2\%$
Time resolution:	$\frac{\sigma_{\text{timing}}}{E} = \frac{1.5}{\sqrt{E}} \oplus 0.5$ ns for E measured in GeV.
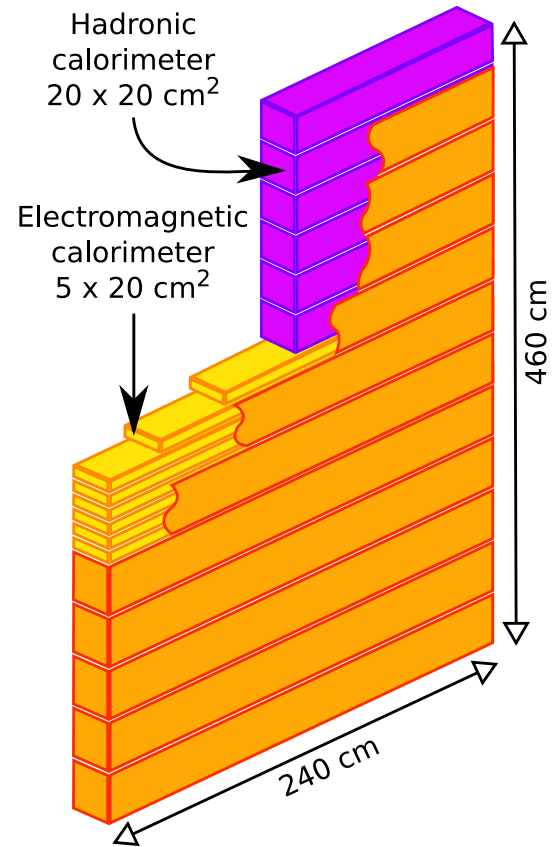
Figure 16: A ZEUS FCAL module.

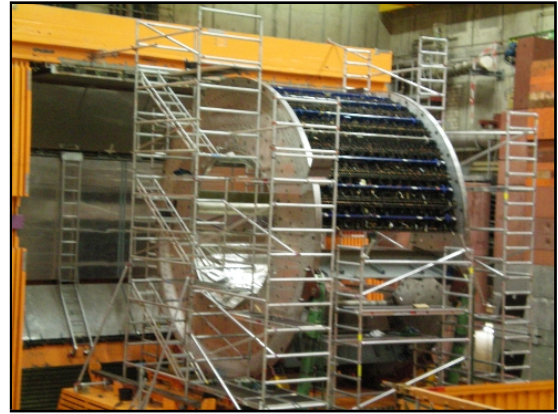*Figure 17: Wavelength shifter installation of a central calorimeter module.*

Figure 18: The ZEUS barrel calorimeter after dismantling had started.

Overview of the three main sections of the calorimeter. Remember, λ is the absorption length:

Section	Name	Dimensions	Depth in terms of λ	Angles covered
Forward end-cap	FCAL	+ 234.4 cm from IP	7.1 λ	$2.2° < \theta < 36.7°$
Barrel	BCAL	Inner radius 134.5 cm	5.1 λ	$36.7° < \theta < 129.1°$
Rear end-cap	RCAL	− 160.2 cm from IP	4.0 λ	$129.1° < \theta < 176.2°$

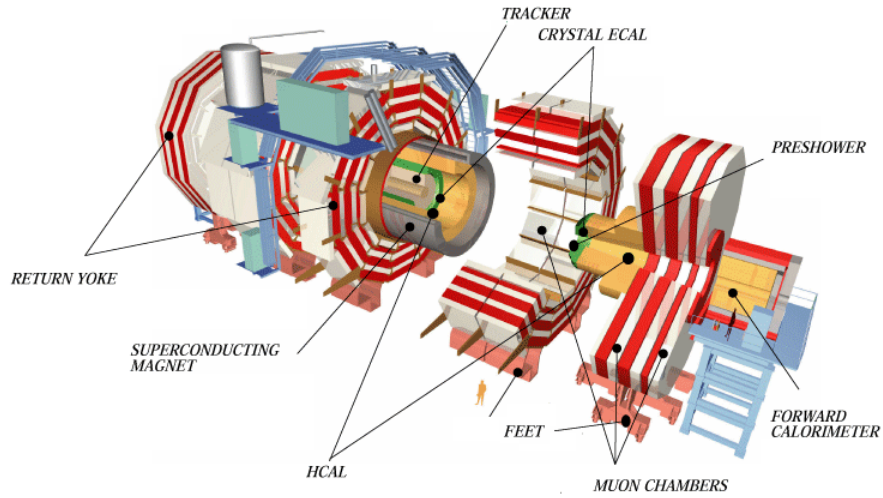## 6.4 Hermetic detector – Compact Muon Solenoid (CMS)

Figure 19: The arrangement of the CMS. In the middle, under the so-called barrel there is a man for scale. (HCAL = hadron calorimeter, ECAL = electromagnetic calorimeter)
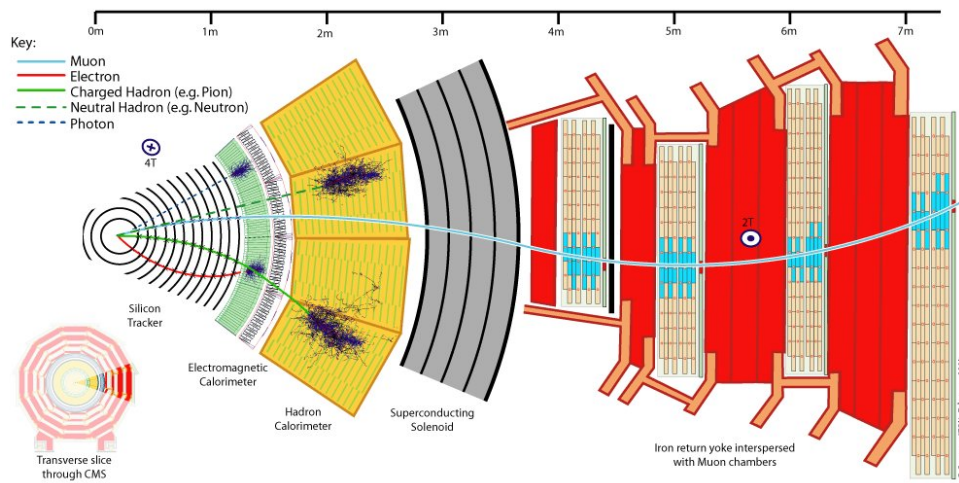

Figure 20: A slice of the CMS showing how $e^{\pm}$, $\mu^{\pm}$, hadrons, neutrons and photons traverse the detector.

Overview of the Compact Muon Solenoid:

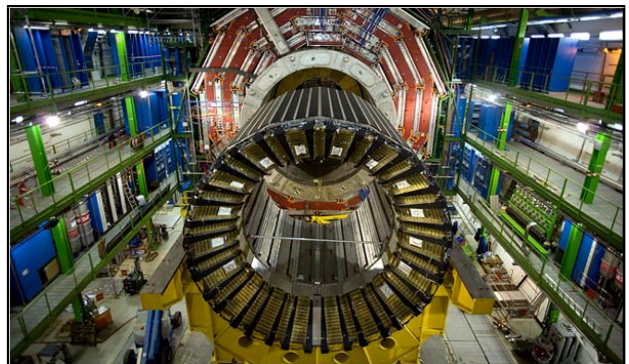|	
Construction dates:	1998 − 2008
Overall length:	21.5 m
Overall diameter:	15.0 m
Total weight:	12,500 tons
Magnetic field:	4 Tesla

Figure 21: The Compact Muon Solenoid.
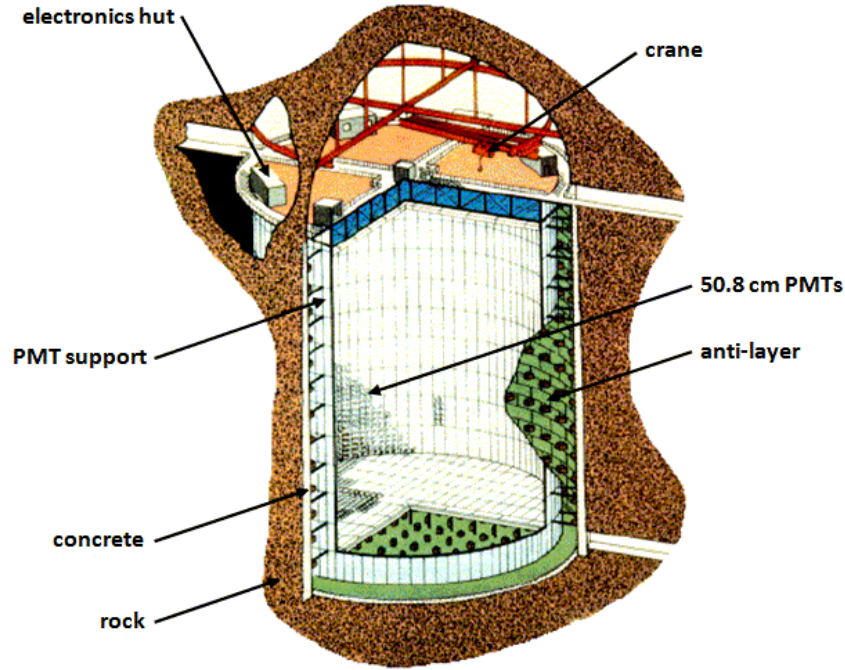
6.5 Ring imaging Čerenkov detector – Super-Kamiokande

Figure 22: View of the Super-Kamiokande detector in the Mozumi Mine in Hida's Kamioka area.

Overview of the Super-Kamiokande detector:

Overall dimensions:	height: 41.4 m, diameter: 39.3 m
Inner detector:	height: 36.2 m, diameter: 33.8 m 11,146 PMTs (diameter: 50.8 cm)
Outer detector:	that volume which remains 1,885 PMTs (diameter: 20.3 cm)
Depth:	1000 m underground
Ultra-pure water:	50,000 tons
Energy resolution:	$\sigma_E = 2.5\%$ (for particles at 1 GeV) $\sigma_E = 16\%$ (for particles at 10 MeV)

Figure 23: Super-Kamiokande construction: checking photo-multiplier tubes (1993 – 1996).

The detector has undergone numerous alterations:

1983	Kamioka NDE	An attempt to observe proton decay.
1985	Kamioka NDE-II	Upgraded to observe solar neutrinos.
1996	Super-K	Observed neutrino oscillations.
2001	Super-K-II	PMTs repositioned after 6600 imploded.
2006	Super-K-III	About 6000 PMTs were restored.

7 Particle identification

7.1 Characteristics of particle events in hermetic detectors

The table below outlines the tracks and shower types expected for a variety of different particle events:

Particles	Signature of event	Tracks	Showers
γ	Neutral photons leave no track in tracking chambers: there will be a small shower without a matched track.	—	Small EM
e^- and e^+	Electrons and positrons leave a track in tracking chambers that matches a small electromagnetic calorimeter shower.	P	Small EM
μ^- and μ^+	These heavier charged particles make it through all the other detectors, leaving minimum ionising signals pointing at the interaction point, eventually stopping at the muon chambers where they deposit their energy.	P + μ	—
ν_e, ν_μ and ν_τ	Neutrinos are the only particles to leave no evidence of their passage through a hermetic detector. Their existence must be inferred by looking for 'missing momentum': conservation of momentum requires that the momentum of the initial colliding beams equals the total momentum of the particles produced, hence the momentum unaccounted for when the momenta of all the visible particles is added up must be the momentum of the neutrino.	—	—
π^0 and η	These light neutral particles will leave no track in tracking chambers: there will be a small calorimeter shower without a matched track.	—	Small hadronic
K^0_S and Λ^0	These heavier neutral particles again leave no track themselves, but soon decay into pair of oppositely charged particles: $K^0 \to \pi^+\pi^-$ and $\Lambda^0 \to p\,\pi^-$. This results in a pair of diverging tracks that begin a distance away from the interaction point equal to the path travelled by the neutral particle: a secondary, or displaced vertex is observed. Displacement of $\sim$ cm is tracked with proportional chambers.	S	Particle decayed
Hadronic jets	Much heavier charged particles deposit very little energy in the tracking chambers, most of their energy is lost in large hadronic calorimeter showers.	—	Large hadronic
$b + c$ quarks	b-tagging: obviously b quarks are not produced as free particles, they are bound in B-mesons, which have a sufficiently long lifetime that they are able to travel some distance before decaying within the detector, hence the decay jet is displaced from the interaction point. The b quark is much heavier than anything it decays into, thus the decay products tend to have higher transverse momentum - making the decay jets wider than usual hadronic showers. Displacement of $\sim$ mm is tracked with silicon detectors.	S	Wide hadronic

In the 'Tracks' column the abbreviations used are: **P** for Primary vertices in the central tracking chamber, **S** for Secondary vertices in the central tracking chamber and **μ** for vertices in the muon chamber.

7.2 Identifying particles from the DELPHI detector at CERN's LEP collider

The images below are real events from the DEtector with Lepton, Photon and Hadron Identification (DELPHI) at the Large Electron Positron (LEP) collider at CERN. [11]

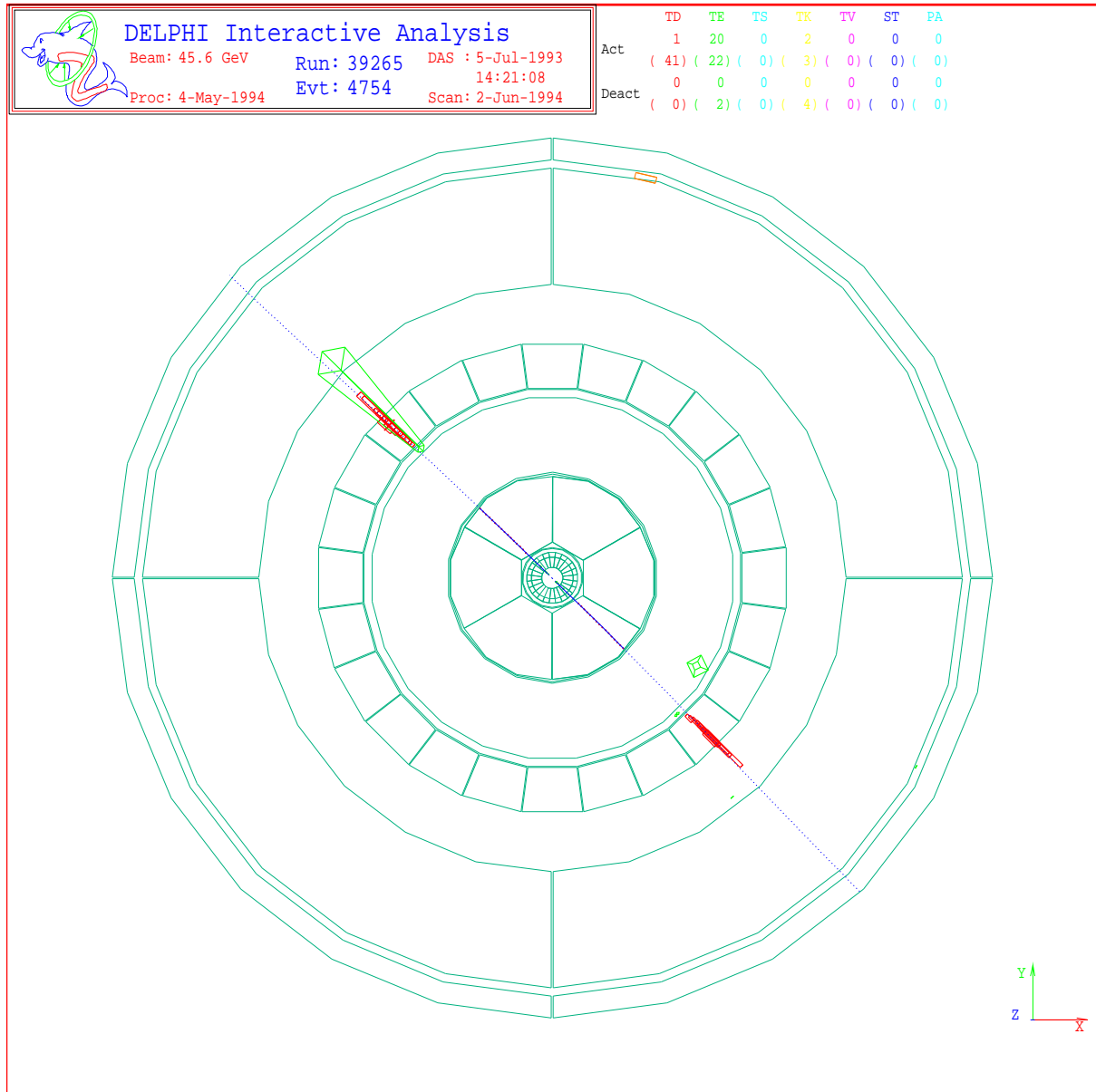### 7.2.1 $e^- e^+ \rightarrow e^- e^+$

Figure 24: $e^- e^+ \rightarrow e^- e^+$

Detector	Observation
Central vertex detectors	Two tracks back to back
Electromagnetic calorimeters	Hits that match the tracks

---

[11]Source: http://delphiwww.cern.ch/delfigs/events/z0ps/z0maxen.html

31

7.2.2 $e^-e^+ \to \mu^-\mu^+$

DELPHI Interactive Analysis

Beam: 45.6 GeV

Proc: 1-Oct-1991

Run: 26154
Evt: 1417

DAS : 25-Aug-1991
21:36:22
Scan: 19-Feb-1992

	TD	TE	TS	TK	TV	ST	PA
Act	26	29	0	2	0	0	0
	(28)	(29)	(0)	(2)	(3)	(0)	(0)
Deact	0	0	0	0	0	0	0
	(0)	(2)	(0)	(2)	(0)	(0)	(0)
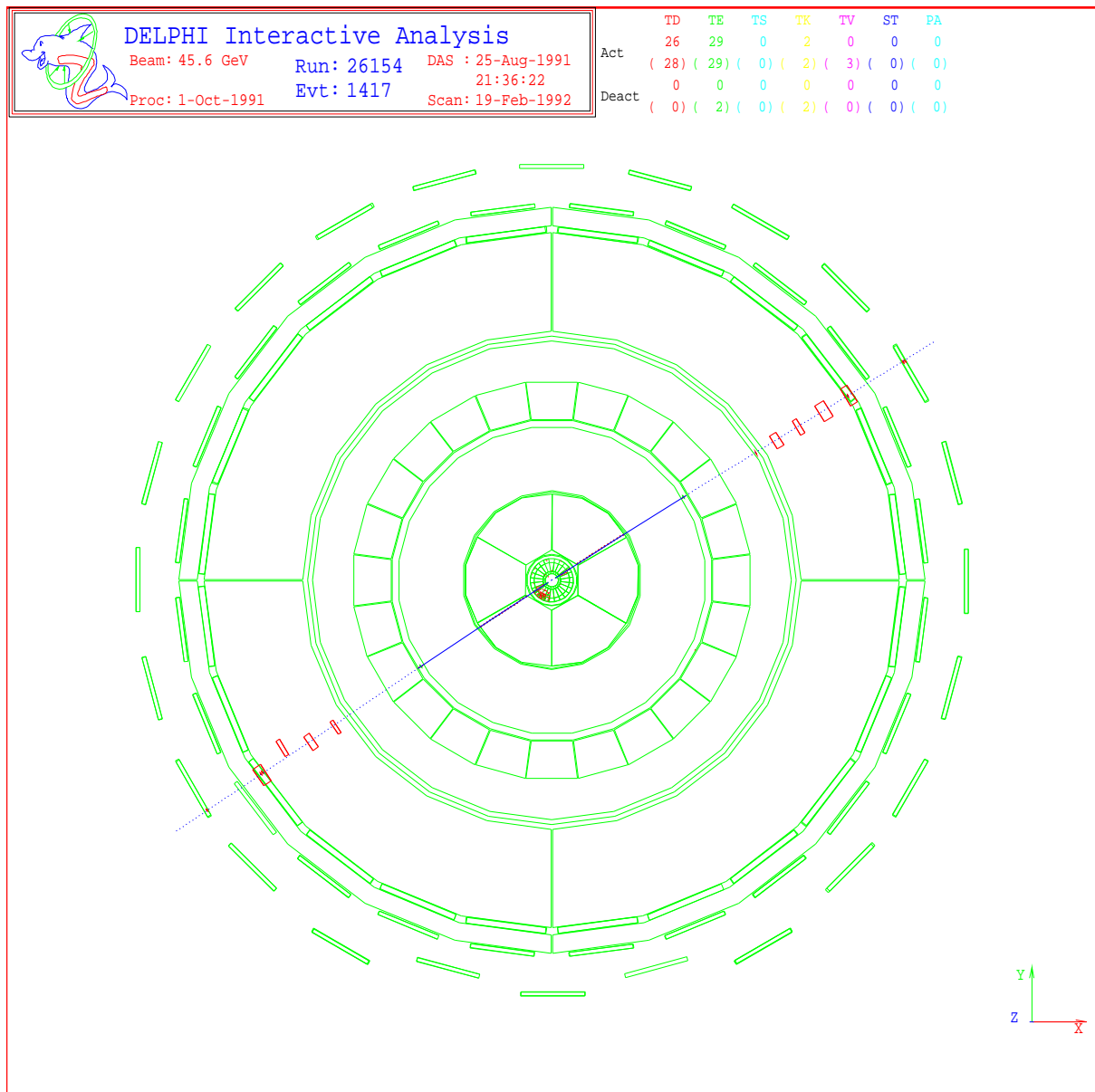
Figure 25: $e^-e^+ \to \mu^-\mu^+$

Detector	Observation
Central vertex detectors	Two tracks back to back
Electromagnetic calorimeters	Nothing
Hadronic calorimeters	Minimum ionising hits
Muon chambers	Hits that match the tracks

32

7.2.3 $e^- e^+ \rightarrow 2$ jets
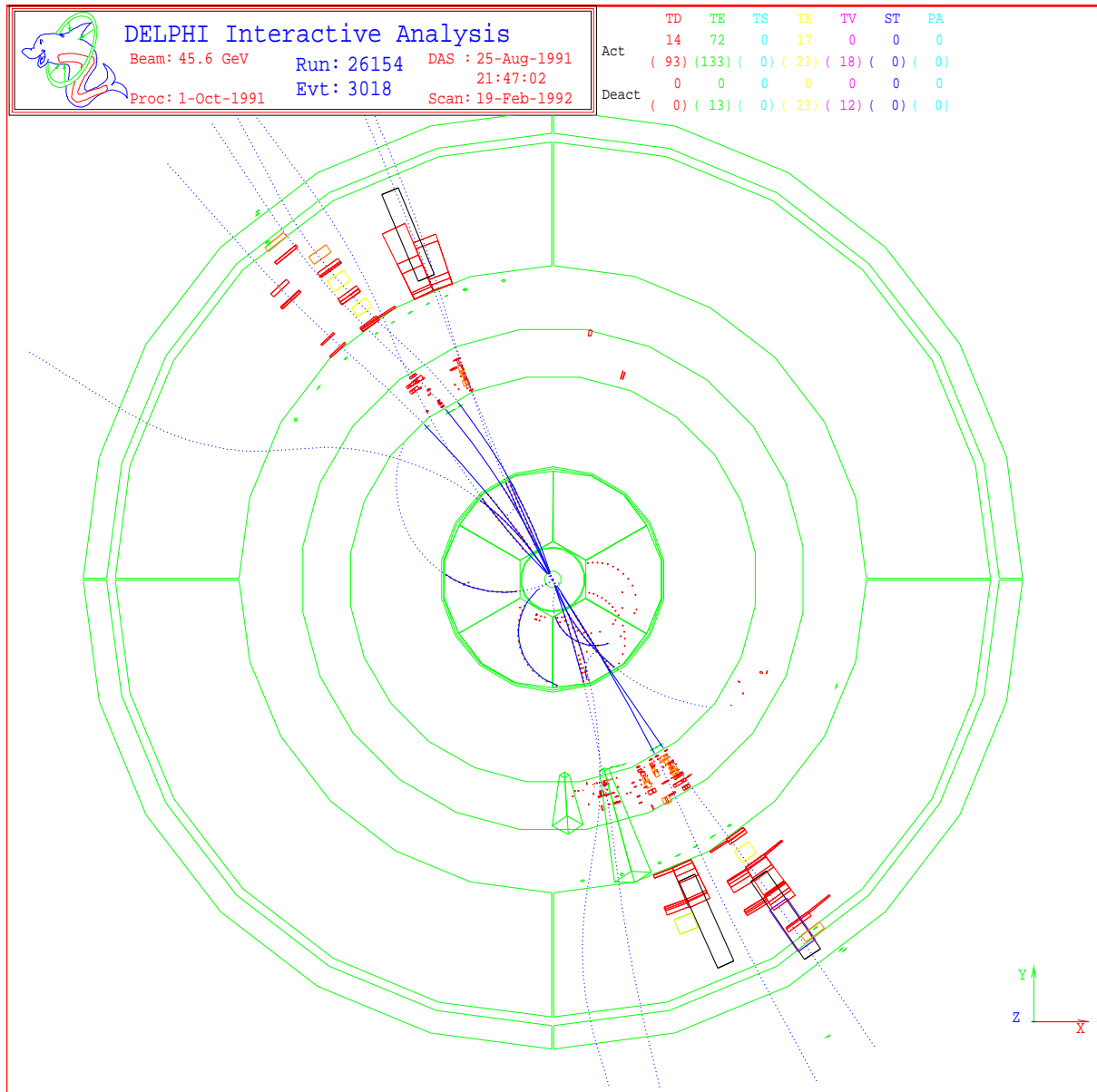
Figure 26: $e^- e^+ \rightarrow 2$ jets

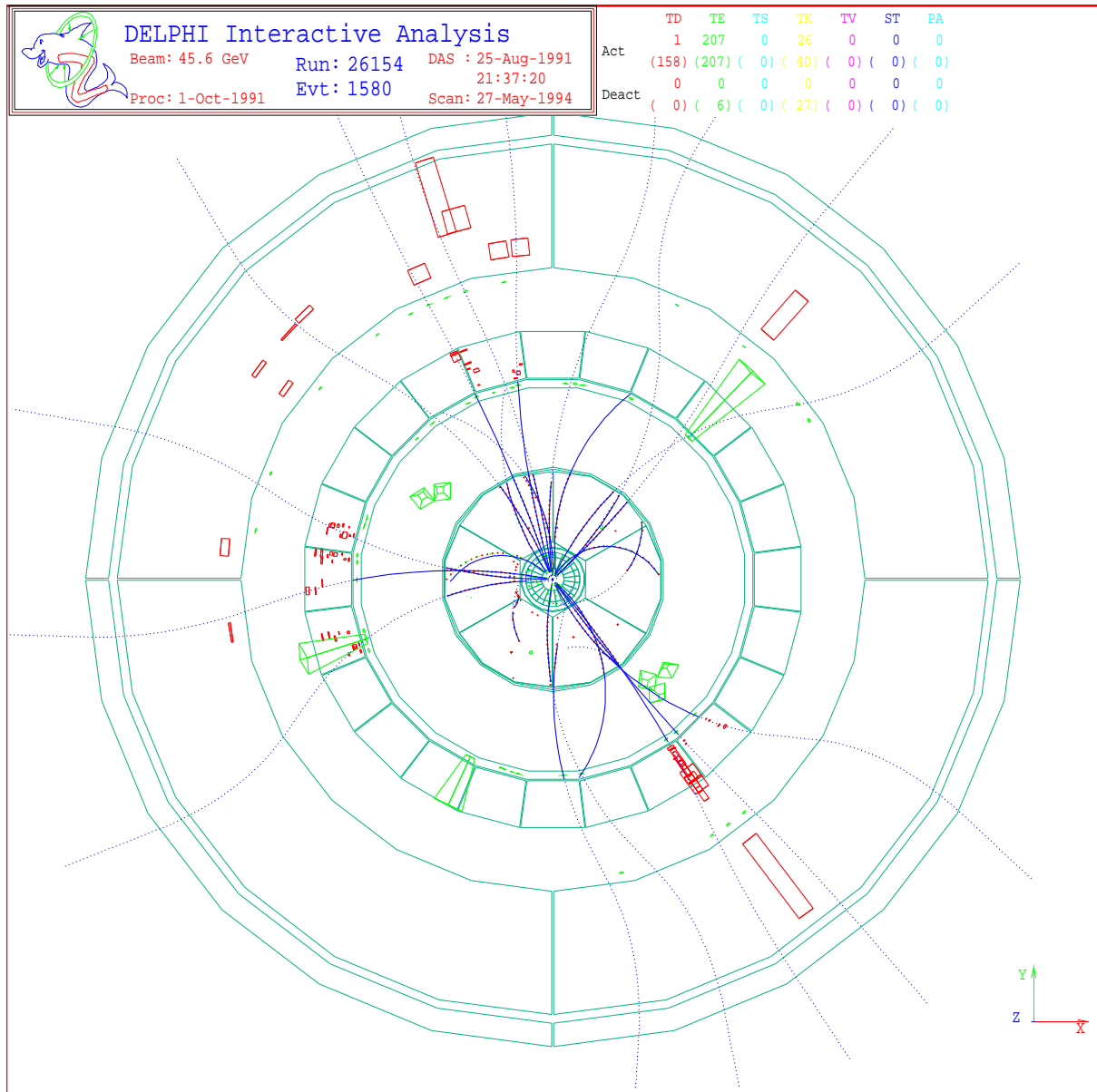| Detector	Observation
Central vertex detectors	Two narrow jets in opposite directions
Electromagnetic calorimeters	Hits that match the tracks
Hadronic calorimeters	Considerable amount of energy deposited

7.2.4 $e^-e^+ \rightarrow$ **3 or 4 jets**

Figure 27: $e^-e^+ \rightarrow 3$ or 4 jets

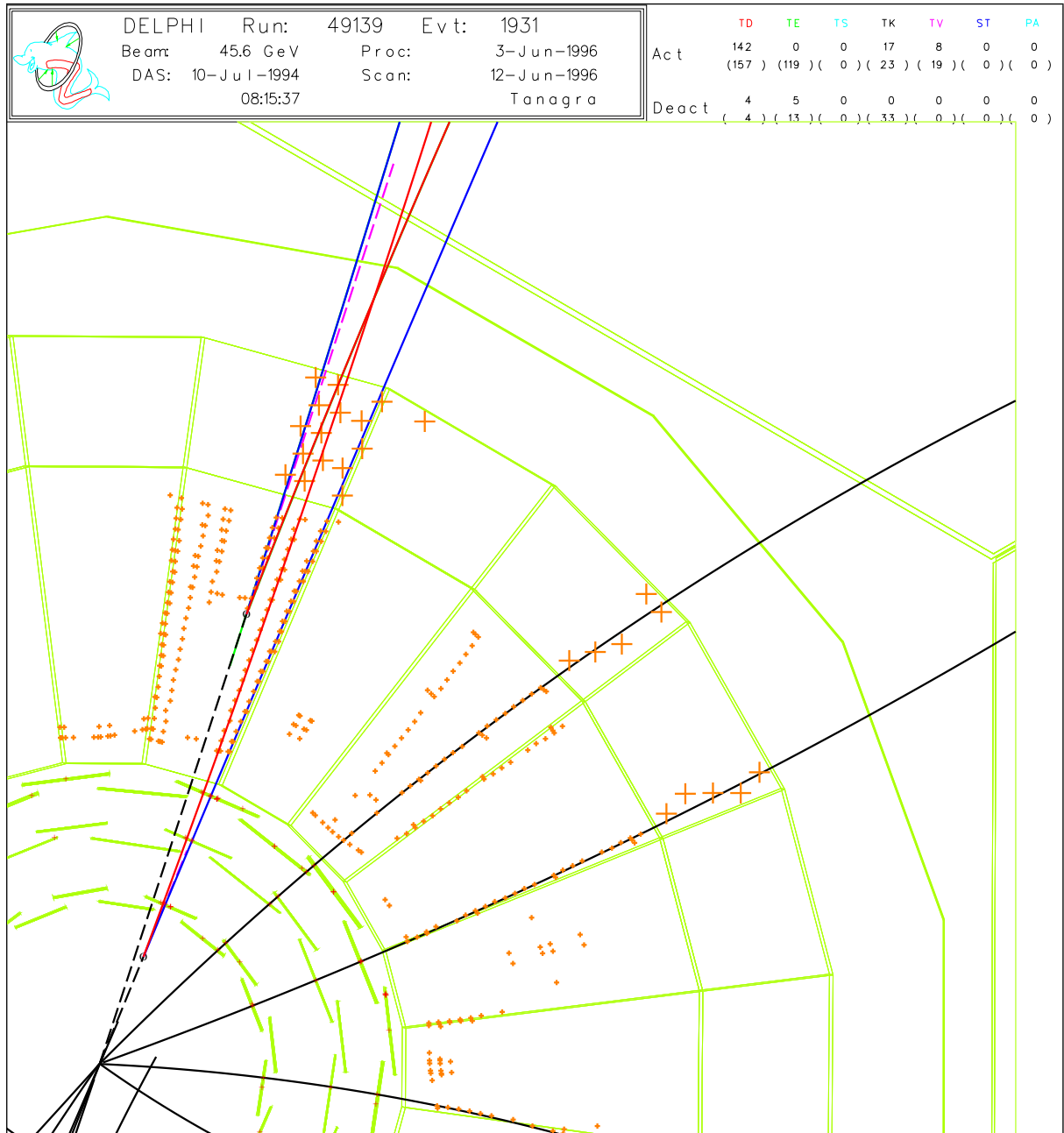| Detector	Observation
Central vertex detectors	A total of 21 different particles seen
Electromagnetic calorimeters	Hits that match the tracks
Hadronic calorimeters	Considerable amount of energy deposited

7.2.5 $e^-e^+ \rightarrow \Lambda\bar{\Lambda}$

Figure 28: $e^-e^+ \rightarrow \Lambda\bar{\Lambda}$

In this event there is a high momentum $\Lambda\bar{\Lambda}$ pair with a small rapidity difference. The lambdas are shown as dashed lines, the outgoing pions as red solid lines and the protons as blue ones. Although there were no track elements reconstructed in the inner detector (intermediate precision tracking) for the Λ that decayed within it (at a radius of 17.9 cm), the vertex has been reconstructed.

The tracks belonging to the other Λ decaying at a radius of 4.4 cm have three associated vertex detector hits.

Three other tracks which are very close to the two lambdas have been erased to make the lambda vertices easier to see.

7.3 Identifying particles from Super-Kamiokande events

The colours in the images [12] below represent the time of arrival of light to individual photomultiplier tubes (PMTs). Short wavelengths (violet and blue) correspond to early arrival times and long wavelengths (orange and red) to late arrival times. A window on the time of light of 30 ns has been applied to eliminate noise and scattered reflected light. The histogram on the right shows the time charge distribution before the applying the window on the time of flight. The size of a given square representing a PMT corresponds to the amount of observed light. There is a maximum size such that squares are always smaller than the distance between PMTs.

7.3.1 Electron events

The **fuzzy ring** with all signals received at roughly the **same time** (the ring is more or less all the same green colour) is an **electron event**.

Since $\sigma_{\text{scatter}} \propto 1/m$, electrons scatter more than muons. So the incident electron produces a shower of photons, electrons and positrons, when it hits the target.

Whilst the photons dont emit any Čerenkov radiation the electrons and positrons all create smaller circles of Čerenkov radiation at an approximately fixed distance from where the electron hit the target.

This gives rise to the fuzzy ring, made up of lots of smaller Čerenkov rings. Since all the electrons and positrons produced started from the same point with roughly the same energy, the PMT signals all occur at the same time; hence the ring is a homogeneous green colour.
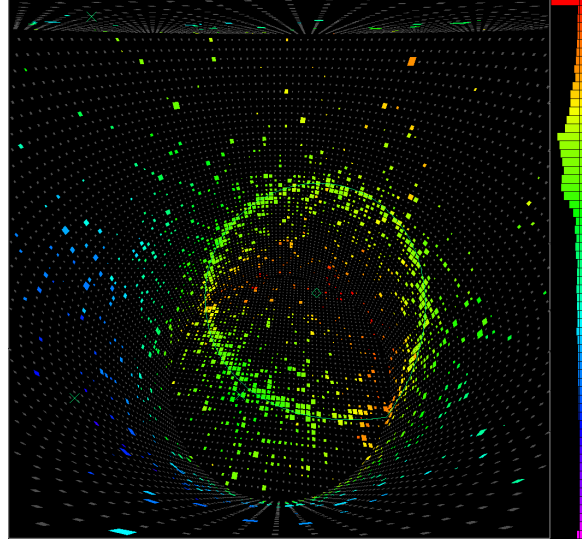

Figure 29: An electron event at Super-K.

7.3.2 Muon events

The **sharply defined ring** with signals occurring at differing times from top left to bottom right is a **muon event**.

The ring is sharply defined compared to the ring from the electron event due to the reduced scattering since $\sigma_{\text{scatter}} \propto 1/m$ and $m_\mu \gg m_e$.

The muon in this image is not quite travelling along the line of sight instead it is moving from the top left, where the blue points (early times) are to the bottom right where the red points (late times) are.
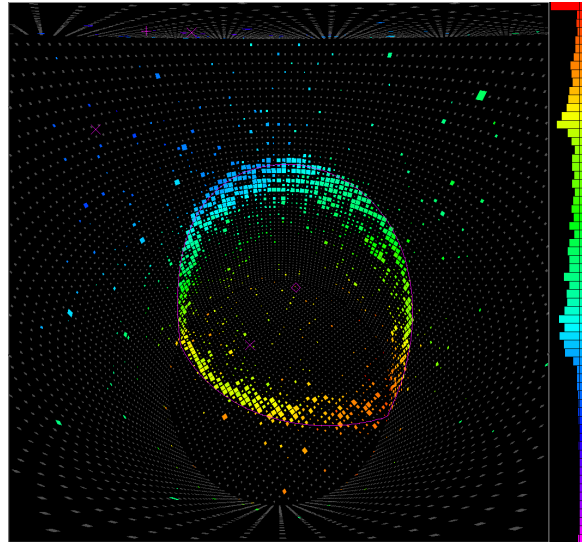

Figure 30: A muon event at Super-K.

---

[12]Source: http://www.ps.uci.edu/~tomba/sk/tscan/compare_mu_e/

7.3.3 Muon decay to electron event

The mean lifetime of a muon is around 2 μs. Since PMTs can record on the nanosecond scale, muons could be observed to decay into electrons and neutrinos according to: $\mu \rightarrow e^- + \bar{\nu}_e + \nu_\mu$.

So if there is an electron event around 2 μs later, it was probably caused by muon decay.

The image to the right shows a muon event, as the sharp blue ring in the top left. Then at a later time a fuzzy green ring appears in the bottom right signifying an electron event.
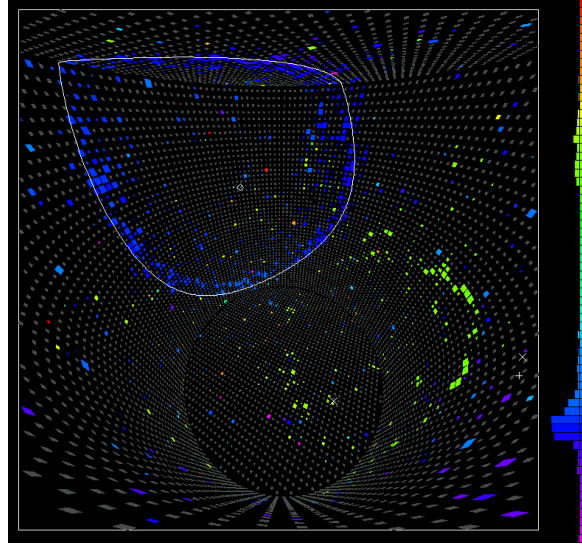

Figure 31: A muon decay event at Super-K.

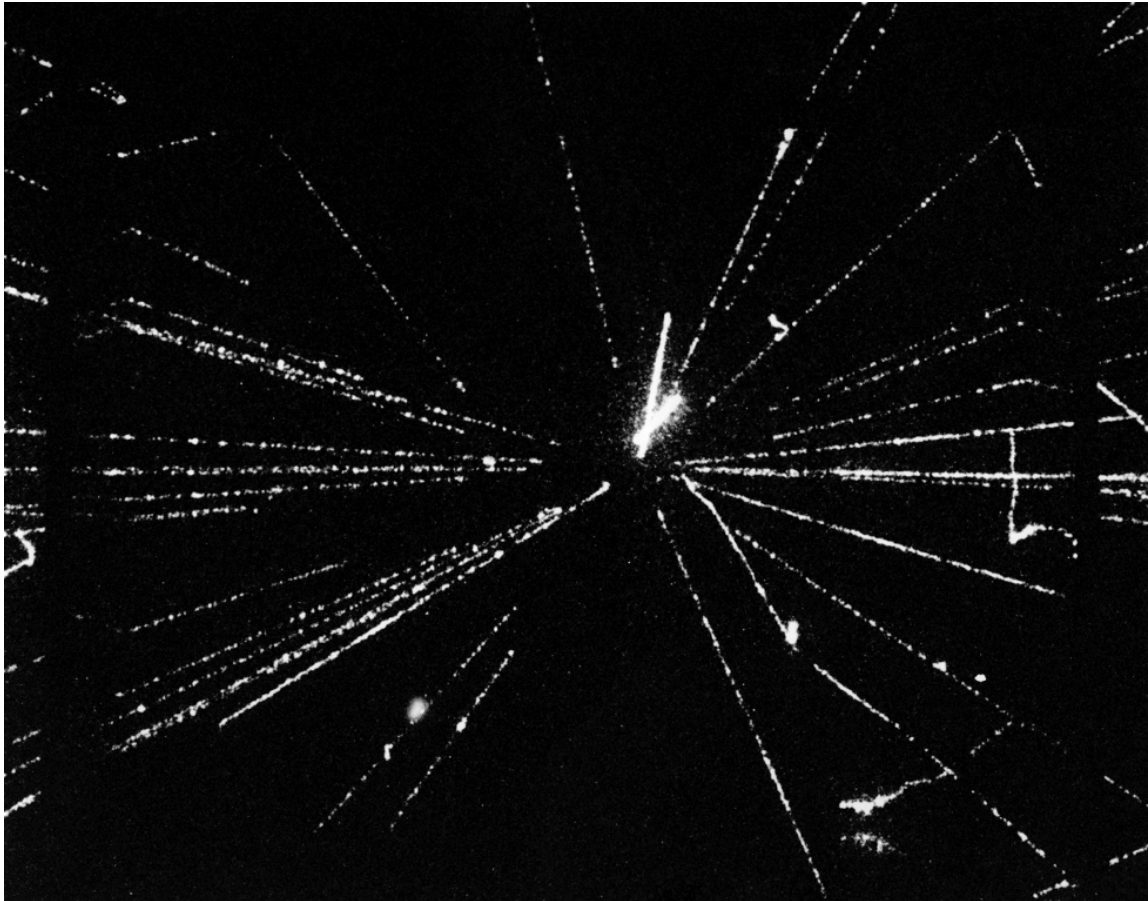## 7.4 Identifying particles from the spark chamber at CERN's SPS

Figure 32: A proton-antiproton interaction at 540 GeV observed using a spark chamber at CERN's Super Proton Synchrotron (SPS) facility in 1982. The identity of the particles produced is anyone's guess.

References

Gaseous ionisation detectors

Data sources: D. Green, The Physics of Particle Detectors (Cambridge University Press, 2000)

W. Blum, W. Riegler & L. Rolandi, Particle Detection with Drift Chambers (Springer-Verlag, 2008)

http://ikpe1101.ikp.kfa-juelich.de/briefbook_part_detectors/PH14pp.html

Spark chambers

Data source: http://www.ep.ph.bham.ac.uk/general/outreach/SparkChamber/text4h.html

Hermetic detectors

Data source: http://www.lancs.ac.uk/users/spc/teaching/py364/introduction.html

Diagram source: http://visits.web.cern.ch/visits/guides/tools/manual/english/Atlas.html

Drift chamber – barrel muon chambers at DELPHI

Data source: http://hepunx.rl.ac.uk/~adye/thesis/html/node14.html
http://delphiwww.cern.ch/delphi$specific/cp/monitor/presenter/help_files/mub_descrip.html

Photo source: http://hands-on-cern.physto.se/hoc_v21en/page_pict/de_muon1.html

Drift chamber with magnetic field – central tracking chamber at ZEUS

Data sources: http://www.pd.infn.it/~longhin/tesidott/html/node30.html
http://www-zeus.desy.de/public/zeus.php3

Photo source: http://www.hep.ucl.ac.uk/~tjf/zctdinst.html

Sampling calorimeter – uranium-scintillator calorimeter at ZEUS

Data sources: http://www.pd.infn.it/~longhin/tesidott/html/node32.html
http://www-zeus.desy.de/public/cal.php3

Photo sources: http://www-zeus.desy.de/img/wls_inst.gif
http://en.wikipedia.org/wiki/File:Zeus_calorimeter.JPG

Hermetic detector – Compact Muon Solenoid (CMS)

Data source: http://en.wikipedia.org/wiki/Compact_Muon_Solenoid

Diagram sources: http://en.wikipedia.org/wiki/File:CMScollaborationPoster.png
http://en.wikipedia.org/wiki/File:CMS_Slice.gif

Photo source: http://www.nytimes.com/2007/05/15/science/15cern.html

Ring imaging Čerenkov detector – Super-Kamiokande

Data source: http://en.wikipedia.org/wiki/Super-Kamiokande

Diagram source: http://atropos.as.arizona.edu/aiz/teaching/a204/lecture11.html

Photo source: http://www-sk.icrr.u-tokyo.ac.jp/sk/gallery/index-e.html